Magyarhoni Földtani Társulat
Földtani Közlöny
Hungarian Geological Society

156/2, 137–154., Budapest, 2026

DOI: 10.23928/foldt.kozl.2026.156.2.137

Zirconolite-bearing symplectites in micro-ijolites: implications for subsolidus processes during ongoing magmatism at Oldoinyo Lengai, Tanzania

Halász, Noémi[1,*], Pekker, Péter[2], Pósfai, Mihály[2,3], Guzmics, Tibor[4], Berkesi, Márta[4,5], †Milke, Ralf[6], M. Tóth, Tivadar[1]

[1]Department of Geology, University of Szeged
[2]Research Institute of Biomolecular and Chemical Engineering, University of Pannonia
[3]HUN-REN–PE Environmental Mineralogy Research Group, Veszprém
[4]Lithosphere Fluid Research Laboratory, Department of Petrology and Geochemistry, Institute of Geography and Earth Sciences, Eötvös Loránd University, Budapest
[5]HUN-REN Institute of Earth Physics and Space Science, MTA FI FluidsByDepth Lendület Research Group, Sopron
[6]Freie Universität Berlin, Germany, † Deceased 7 October 2022
*Corresponding author: halasznoemi94@gmail.com

Cirkonolit-tartalmú szimplektitek mikro-ijolitokban: jelentőségük a szubszolidusz folyamatok értelmezésében az Oldoinyo Lengai (Tanzánia) területén zajló magmatizmus során

Összefoglalás

Az Oldoinyo Lengai vulkánból származó olivin-flogopit mikro-ijolit kőzetek komplex magmás folyamatokat rögzítenek. Ezekben szimplektitek formájában megőrződtek szubszolidusz-reakciók bizonyítékai is. A kutatás során vizsgált szimplektitek alkotói lamellás formában jelennek meg bimodális szemcseméret-eloszlással: a diopszid és az ilmenit egyaránt előfordul durva- (2–3 μm) és finomszemcsés (<2 μm) lamellákban, míg a cirkonolit kizárólag durva (~5 μm), a ritkaföldfém-perovszkit pedig közepes méretű lamellákban jelenik meg. A bimodális eloszlás eltérő hőmérsékleteken történő kialakulást tükröz. A mikro-ijolit kialakulását leginkább két paragenezis váltakozása határozta meg: magas hőmérsékleten a „diopszid-paragenezis" (970–1070 °C), míg alacsonyabb hőmérsékleten az „egirin-augit-paragenezis" (700–850 °C). A durvaszemcsés szimplektitlamellák képződése a magasabb hőmérsékletű paragenezishez köthető, míg a finomszemcsés lamellák az alacsonyabb hőmérsékletű paragenezis során jöttek létre. A szimplektitek feltehetően az olivin és a titanit közötti szubszolidusz reakció eredményeként alakultak ki, amelynek reakciótermékei a diopszid, az ilmenit és a cirkonolit. Utóbbi a titanit lebomlása során felszabaduló ZrO_2-ból (0,4–0,8 tömeg%) jöhetett létre. Transzmissziós elektronmikroszkópos vizsgálatok kimutatták, hogy a cirkonolit kristályok összetétele közel ideális, a cirkonolit-2M politípushoz tartoznak, és két ikerdoménből épülnek fel. Az ikertengely az [110] iránnyal párhuzamos, ami 180°-os elfordulást eredményez, a kontakt ikersík párhuzamos a (001)-gyel. Eredményeink rávilágítanak arra, hogy a szubszolidusz folyamatok egyidejűleg is működhetnek a magmás kristályosodással. Ennek ékes bizonyítékai az Oldoinyo Lengai olivin-flogopit mikro-ijolit kőzeteiben megfigyelhető szövetek és ásványegyüttesek.

Tárgyszavak: szimplektit, Oldoinyo Lengai, ijolit, cirkonolit, szubszolidusz-reakciók, TEM

Abstract

Olivine-phlogopite micro-ijolite enclaves from Oldoinyo Lengai record complex, multistage magmatic processes. These rocks preserve evidence of subsolidus reactions demonstrated by the development of symplectites. The symplectites studied here are present in lamellae and display bimodal grainsize distributions of their constituent phases: diopside and ilmenite occur as both coarse- (2–3 μm) and fine-grained (<2 μm) lamellae, whereas zirconolite forms only in coarse- (~5 μm) and REE-perovskite medium-sized lamellae. The bimodality reflects crystallization at different temperatures. For the thermal evolution of the micro-ijolite, two parageneses have been discovered: at high-temperature the "diopside-paragenesis" (970–1070 °C), whereas and at lower-temperature "aegirine-augite-paragenesis" (700–850 °C) was formed. Coarse-grained lamellae's formation corresponds to the high-T formation, and the fine-grained ones formed during the low-T evolution steps. The symplectites likely formed through a subsolidus reaction between olivine and titanite, forming diopside, ilmenite and zirconolite as reaction products. Titanite's breakdown in this reaction and thus the deliberation of its ZrO_2 (0.4–0.8 wt%) were the major factors controlling zirconolite formation. Transmission electron microscopy analyses revealed that zirconolite crystals are near-ideal in composition, belong to the zirconolite-2M polytype and composed of two twin domains. The twin axis is parallel to [110], resulting in 180° rotation around the [110], with the contact plane parallel to (001). Our findings demonstrate that subsolidus processes may operate simultaneously with magmatic crystallization, as recorded by the textures and mineral assemblages within these rocks from Oldoinyo Lengai.

Keywords: symplectites, Oldoinyo Lengai, ijolite, zirconolite, subsolidus reactions, TEM

Introduction

Although the active Oldoinyo Lengai is primarily known for its recently erupting natrocarbonatite lavas (YAXLEY et al. 2022 and references therein), the evolution of the underlying alkaline plutonic rocks remains comparatively poor, despite their critical role in the understanding of East African Rift magmatism. The diverse suite of plutonic rocks already described beneath Oldoinyo Lengai (e.g., pyroxenite, urtite, ijolite) suggests a complex magmatic system at sub-volcanic level associated with the evolution of the volcano (KELLER & KRAFT 1990, DAWSON et al. 1995, DAWSON 2008, CARMODY 2012, SEKISOVA et al. 2015, HALÁSZ et al. 2023). Evidence of multi-stage magmatic evolution is well preserved in the olivine-phlogopite micro-ijolites (DAWSON 2008, CARMODY 2012, SEKISOVA et al. 2015, HALÁSZ et al. 2023). However, the subsolidus processes associated with these rocks have received limited attention, even though they are essential for understanding their complex evolutionary history as symplectites are vital markers for subsolidus (re)crystallization processes (VERNON 2004). Although symplectites are commonly associated with metamorphic processes, they are not restricted to regional metamorphic environments. Similar microstructures may also form under magmatic to subsolidus conditions through solid-state reactions between primary igneous minerals or as a result of mineral–melt interaction during late-stage crystallization.

In this study, symplectites contain minerals such as zirconolite and REE-bearing perovskite. Zirconolite-bearing symplectites have not previously been described from Oldoinyo Lengai rocks. However, they may provide important insights into the interaction between subsolidus processes and ongoing magmatic crystallization, as well as into the role of titanite breakdown in zirconium mobilization and zirconolite formation. Here we present detailed textural and mineralogical features of symplectites occurring in olivine-phlogopite micro-ijolites. We estimate the formation temperature, the significance of the zirconolite-bearing symplectite formation coeval with the igneous crystallization. We demonstrate that magma chamber processes can be the host of subsolidus reactions besides the dominant magmatic evolution through the case study of symplectite formation in ijolite rocks underneath Oldoinyo Lengai. The aim of this study is to characterize the mineralogy and microstructural features of these symplectites, and to constrain their formation mechanisms in relation to the host rock evolution.

General overview of zirconolite

Zirconolite is a zirconium-titanium oxide with the nominal, IMA-approved composition formula:

$$(Ca,Y)Zr(Ti,Mg,Al)_2O_7$$

It occurs as an accessory mineral in a variety of rock types, including metamorphic (e.g., granulite, contact metamorphic rocks, metamorphosed breccia, metacarbonates), magmatic (e.g., kimberlites, ultrabasic cumulates, nepheline syenites, carbonatites), and metasomatized rocks (WILLIAMS et al. 2011). In addition, zirconolite has been identified in lunar and meteoritic samples, though it is most commonly associated in magmatic carbonatites (WILLIAMS et al. 2011). Occurrence of zirconolite is additionally documented from several areas where alkaline and carbonatitic complexes worldwide, including Arbarastakh, Russia (KRUK et al. 2021); Eifel, Germany (DELLA VENTURA et al. 2000, ZUBKOVA et al. 2018); Vico, Italy (BELLATRECCIA et al. 2002); Afrikanda, Russia; Amba Dongar, India; Araxa, Brazil; Cummins Range, Australia, Howard Creek, Canada; Jacupiranga, Brazil; Mabouine, Gabon; Sokli, Finland; Phalaborwa, South Africa (WILLIAMS & GIÉRE 2001); Larvik, Norway (HAIFLER et al. 2020); Evate, Mozambique (HURAI et al. 2018). Zirconolite is also used as a ceramic waste form designed to immobilize the high-level radioactive waste from reprocessing spent fuel from nuclear reactors (KESSON et al. 1983). Zirconolite formation can be attributed to various geologic processes such as crystallization from a silica-poor melt, solid-melt interaction, metamorphism and metasomatism (GIERÉ 1986, 1990; GIERÉ & WILLIAMS 1992; HEAMAN & LECHEMINANT 1993; RIED 1994; GIERÉ et al. 1998; BELLATRECCIA et al. 2002).

Zirconolite has five known polytypes (BAYLISS et al. 1989), three of which (zirconolite-2M, zirconolite-3T, zirconolite-3O) have been reported in natural samples (MAZZI & MUNNO 1983, WHITE et al. 1984, BAYLISS et al. 1989), while two additional polytypes (zirconolite-4M, zirconolite-6T) have been synthesized experimentally (SMITH & LUMPKIN 1993, COELHO et al. 1997). Among the three natural polytypes, zirconolite-3O is a three-layered orthorhombic, zirconolite-3T is a three-layered trigonal, and zirconolite-2M is a two-layered monoclinic variety (BAYLISS et al. 1989, GIERÉ et al. 1998). In the monoclinic crystal structure, the two layers are related to each other by a 180° rotation and interlayer stacking vectors [130] and [$\underline{1}$30] with a 2.1 Å displacement (WHITE 1984, WHITE et al. 1984, BAYLISS et al. 1989). The monoclinic structure of zirconolite is closely related to those of fluorite and pyrochlore; it can be regarded, for instance, as an anion-deficient superstructure based on the fluorite structure (ROSSELL 1980).

Zirconolite often exhibits chemical zonation. The composition of zirconolite can be very diverse, as more than thirty elements (Mg, Al, Si, Ca, Ti, Mn, Fe, Zr, Nb, Hf, Ta, W, Pb, Zn, Sr, Ba, rare earth elements (REE: Y, La, Ce, Pr, Nd, Gd); and actinides (ACT: Th, U) may be present at concentrations of 0.1 to 1.0 (in wt%) (DE HOOG & VAN BERGEN 1997, LUMPKIN et al. 1994). Pb is occasionally present in some samples (up to 1.5 wt% PbO), and its concentration correlates with those of Th and U, as most of the Pb is radiogenic (LUMPKIN et al. 1994, GIERÉ et al. 1998). REE and ACT element enrichment causes twinning in some zirconolites (GIERÉ et al. 1998). Owing to its U and Th content, zirconolite can be suitable for age estimation, for example by the methods of WANG et al. (2021).

While we assume this is the first report of zirconolite occurrence from Oldoinyo Lengai, it was already reported from the neighbouring Kerimasi volcano (*Fig. 1*), as part of

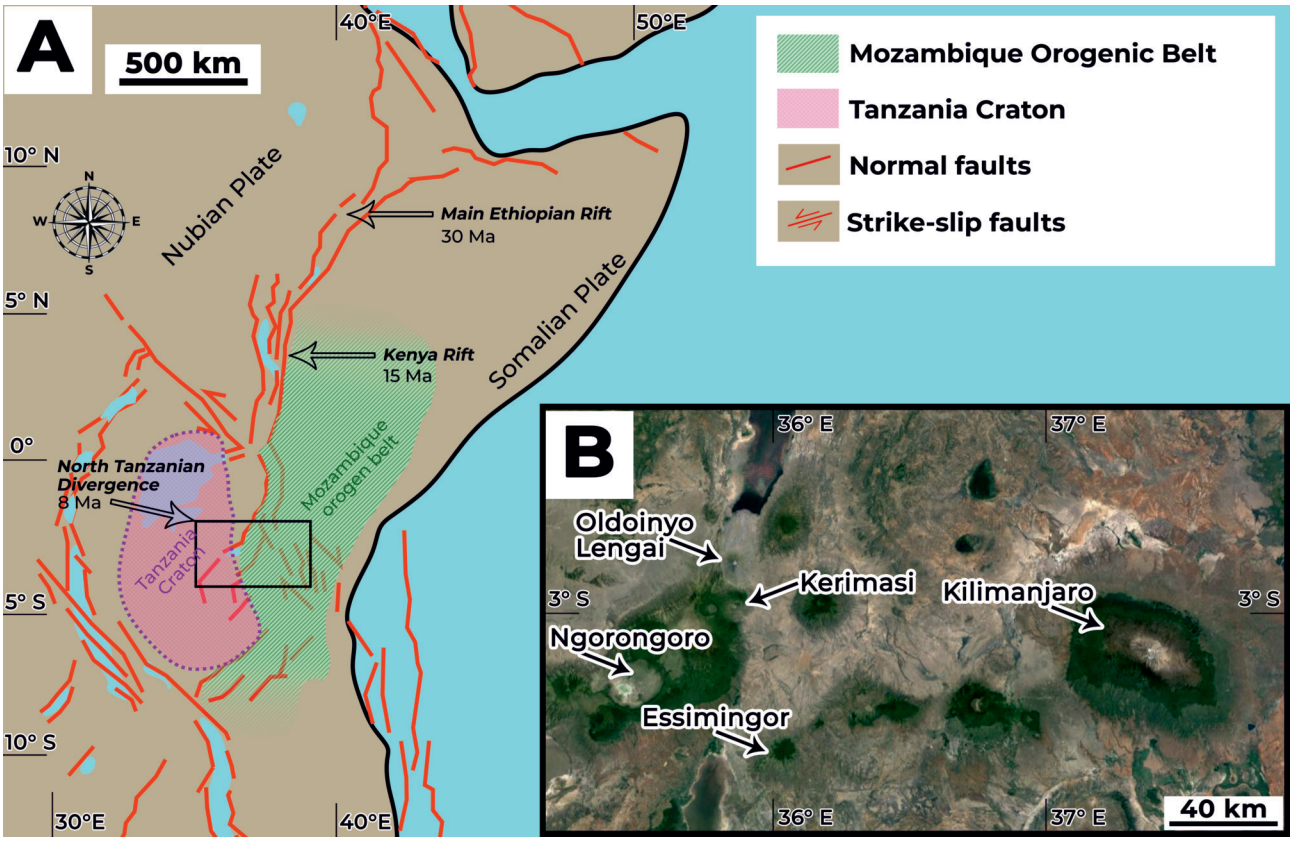

Figure 1. A – Map of the East African Rift system; B – inset satellite image of the North Tanzanian Divergence, the study area. Figure A was modified after Conti et al. (2021).

1. ábra. *A – a Kelet-afrikai-árokrendszer sematikus térképe (Conti et al. 2021 után módosítva); B – műholdkép az észak-tanzániai vulkanikus provinciáról, melyen a kutatási terület található.*

a magnetite-hosted carbonate melt inclusion along with baddeleyite, perovskite and olivine (Káldos et al. 2015).

Geological background

The East African Rift System extends approximately 3,700 km in a north-south direction from the Gulf of Aden to Mozambique (*Fig. 1a*). Based on gravity anomaly data, seismic tomography, modelling and geochemistry (Brown & Girdler 1980, Simiyu & Keller 1997, Lithgow-Bertelloni & Silver 1998, Ebinger & Sleep 1998, Rogers et al. 2000), the plate motion is interpreted to result from continental rifting, possibly governed by one or more impinging mantle plumes beneath the region. These plumes have also resulted in lithospheric thinning, causing the Moho depth to be shallow at 40 to 35 km (Prodehl et al. 1994).

The East African Rift System, a significant geological feature, splits the African plate into the Nubian and the Somalian plates along two tectonically different rift branches, the Western Rift (Albertine-Rift) and the Eastern Rift (Gregory-Rift). The Tanzania Craton (*Fig. 1a*) plays a key role in controlling the rift geometry and development (Ebinger & Sleep 1998, Corti 2012, Wood & Guth 2014). The magmatism occurs predominantly at the contact zone between the Archaean Tanzanian Craton and the Mozambique Belt (Mana et al. 2015).

Rift-related volcanism started around 30 Ma ago in the northern parts of the Eastern Rift in Ethiopia, continued 15 million years ago in Kenya, and then 8 million years ago along the North-Tanzanian Divergence, with the first evidence recorded from Essimingor (*Fig. 1a, b*). The North Tanzanian Divergence is a ~200 km wide zone extending from the caldera of Ngorongoro to the Kilimanjaro volcano (Baker et al. 1971, Dawson 2008) (*Fig. 1a, b*).

The Oldoinyo Lengai volcano is dominantly built by phonolitic and nephelinitic rocks (Donaldson et al. 1987, Klaudius & Keller 2006, Dawson 2008). In addition to the peralkaline volcanic rocks, the volcano also brings a variety of plutonic rock types to the surface and uniquely produces natrocarbonatite lava (Donaldson et al. 1987, Klaudius & Keller 2006, Dawson 2008). At Oldoinyo Lengai, the most common plutonic rocks are pyroxenite, urtite and ijolite, occurring as blocks or bombs hosted by nephelinite lavas and pyroclasts (Dawson 2008). Oldoinyo Lengai ijolites are divided into two distinct types: archetypal coarse-grained plutonic ijolite composed of clinopyroxene, nepheline, titanite, magnetite, perovskite, biotite, ±garnet, ±wollastonite, and olivine-phlogopite ijolite containing clinopyroxene, nepheline, titanite, magnetite, perovskite, biotite, ±garnet, ±wollastonite, phlogopite and olivine (Dawson et al. 1995, Dawson 2008, Sekisova et al. 2015). Some olivine-phlogopite ijolite samples (Dawson et al. 1995, Dawson 2008, Carmo-

DY 2012, SEKISOVA et al. 2015) should not be termed ijolite *sensu stricto* as these samples are texturally different and do not exhibit the typical allotriomorphic granular textures of plutonic ijolites. Therefore, referring to these rocks simply as "olivine-phlogopite ijolite" could lead to misleading petrogenetic comparisons. Although there is currently no IUGS-approved term for this fine-to-coarse-grained assemblage, in a previous study (HALÁSZ et al. 2023) we proposed that these distinctive rock types be classified as *olivine-phlogopite micro-ijolite*. Olivine–phlogopite micro-ijolite enclaves (previously described as xenoliths in the literature) from Oldoinyo Lengai record complex, multistage magmatic processes. The term "enclave" is used here to emphasize their co-magmatic origin and genetic relationship with the host melt and to avoid the implication of an exotic source inherent in the term "xenolith." The subject of the present research – zirconolite-bearing symplectites – is found in these micro-ijolites and consists of ilmenite, diopside, zirconolite, and occasionally REE-bearing perovskite.

Studied samples and analytical methods

Sampling and thin section preparation

Rock samples were collected by Tibor GUZMICS during a 2016 field trip at Oldoinyo Lengai, Tanzania. From approximately 100 kg of collected material, 40 kg of fresh and representative hand specimens were selected, including olivine–phlogopite micro-ijolite (~13%). Samples were collected at latitude 2.749002° S and longitude 35.890602° E, and five representative specimens from the OL-15 series (HALÁSZ et al. 2023) were selected for detailed study. All investigated samples display uniform textural and mineralogical characteristics and are therefore described collectively. Polished thin sections were prepared following standard procedures at the University of Szeged, Department of Geology. Petrographic observations (made using Brunel-SP-300-P and Olympus BX 41 optical microscopes) confirmed the homogeneity of the studied material and guided the selection of analytical sites for in-situ mineral chemical analyses.

In-situ mineral chemistry by electron beam

In-situ mineral compositions were determined using both SEM–EDS and EPMA techniques. Zirconolite, ilmenite and perovskite in symplectitic intergrowths were analyzed by EDS using a Hitachi TM4000Plus scanning electron microscope equipped with an Oxford Xplore Compact 30 SDD detector at the ELTE FS-RICF. Analyses were performed at 15 kV accelerating voltage with short counting times, following the analytical approach validated by BERKESI et al. (2020). Element concentrations were corrected using the XPP algorithm and recalculated to oxide weight percentages assuming stoichiometry; totals were normalized to 100 wt%, with Fe reported as FeO^T. Mineral formulae were calculated in atoms per formula unit (apfu) following HAIFLER et al. (2021). Major element compositions of associated minerals were measured by wavelength-dispersive EPMA using a JEOL JXA-8200 Superprobe at the Free University Berlin. Analyses were conducted at 15 kV accelerating voltage and 20 nA beam current, with ZAF correction using the PAP algorithm. Analytical totals within 100.0 ± 1.5 wt% were considered acceptable. Mineral formulae were calculated on the basis of fixed number of oxygen atoms for each mineral phase (4 O for zirconolite and ilmenite, 6 O for diopside, and 5 O for perovskite) following established IMA-approved classification schemes.

High-resolution transmission electron microscopy (HR-TEM)

Focused ion beam (FIB) lamellae were prepared using a Thermo Fisher Scientific SCIOS-2 dual-beam FEG-SEM/FIB at the HUN-REN Centre of Energy Research, Budapest. HR-TEM investigations were carried out at the University of Pannonia using a Thermo Fisher Scientific Talos F200X G2 microscope operated at 200 kV and equipped with a Super-X EDS system. Bright-field, high-resolution images, selected-area electron diffraction (SAED) patterns, and EDS analyses were acquired in TEM mode, while HAADF imaging and STEM–EDS element mapping were performed in STEM mode. Zirconolite polytypes and planar defects were identified primarily using SAED and HAADF imaging, whereas chemical compositions were determined from EDS area analyses and element maps using Cliff–Lorimer k-factors. Compositional variations between crystal cores and rims were identified by integrating summed spectra from selected areas.

Results

Petrography and mineral chemistry of olivine-phlogopite micro-ijolite enclaves

For a detailed petrographic description and discussion of the evolution of the olivine-phlogopite micro-ijolite rocks, see HALÁSZ et al. (2023). In this paper, only a concise summary of their petrology is provided, as the main focus is on the subsolidus reactions and their products: symplectites. Nevertheless, to better understand the formation and evolution of the symplectite, it is necessary to understand the host micro-ijolites.

The symplectite-hosting studied samples consist of olivine-phlogopite micro-ijolite enclave enclosed by nephelinite lava rock (*Fig. 2a*). The olivine-phlogopite micro-ijolite part is built up by three textural domains: the groundmass, phlogopite phenocrysts (mg# = 81–85) and olivine crystal with double coronas around them (*Fig. 2a*) (HALÁSZ et al. 2023).

The groundmass is medium-grained (0.05–2 mm) with zoned clinopyroxene, nepheline, titanite, and minor pseudomorphic analcime crystals. Clinopyroxene occurs as zoned phenocrysts; some crystals are euhedral, whereas others have

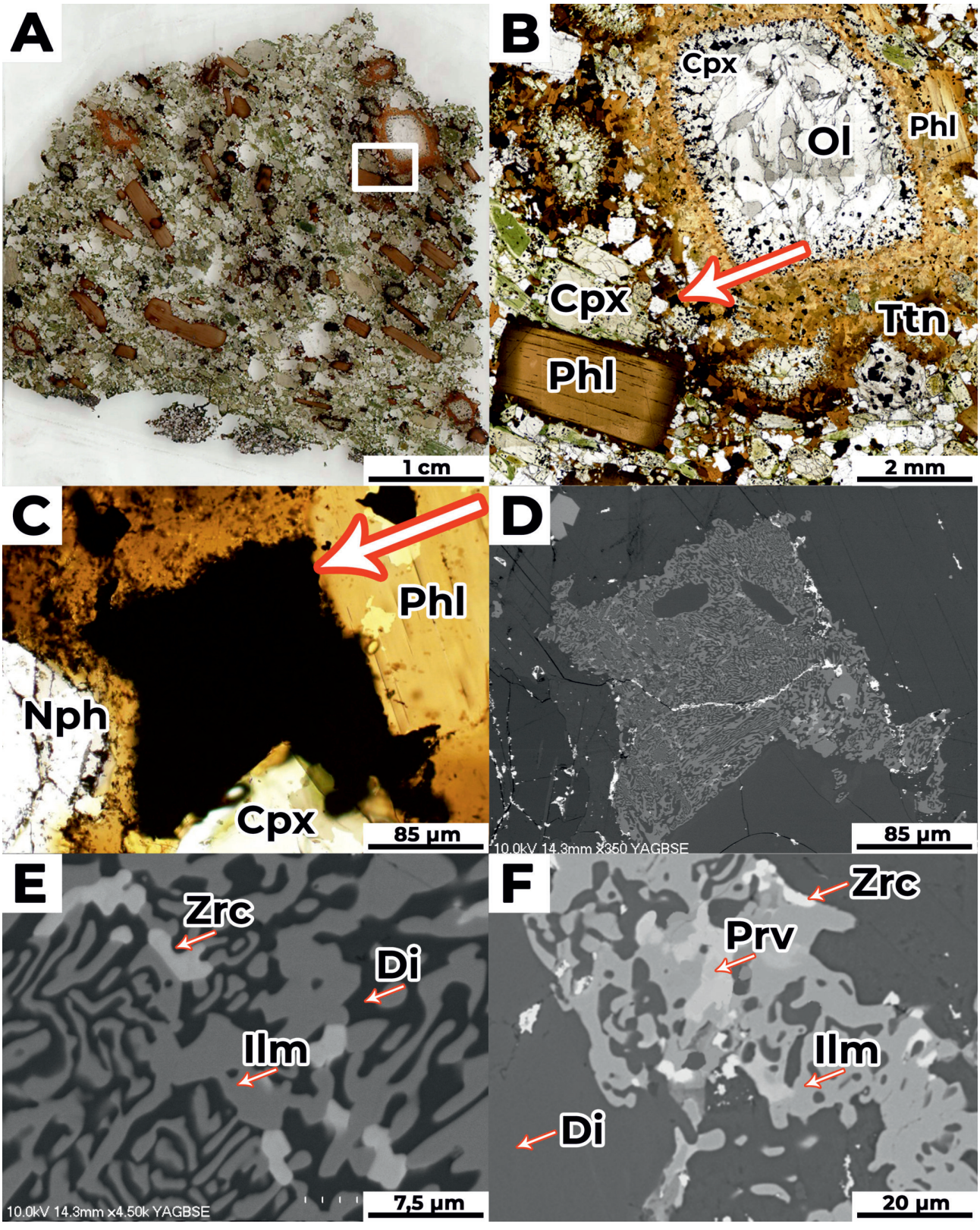

Figure 2. The studied olivine-phlogopite micro-ijolite enclave, Oldoinyo Lengai, Tanzania. A – Optical microscope image of a representative symplectite; B – inset of A image, showing a double corona; C – petrographic image of a symplectite; D – BSE image of a symplectite shown in C; E – close-up of a symplectite; F – close-up of a symplectite containing perovskite. Abbreviations cf. Whitney & Evans (2010), plus Zrc – zirconolite.

2. ábra. *Az Oldoinyo Lengairól (Tanzánia) származó, vizsgált olivin-flogopit mikro-ijolit enklávé. A – egy reprezentatív szimplektit helyének optikai mikroszkópos képe; B – az A képrészlet kinagyított részlete, mely bemutatja a szimplektitet tartalmazó kettőskoronás szöveti elemet; C – egy szimplektit petrográfiai képe; D – a C képen látható szimplektit BSE-képe; E – egy szimplektit közeli felvétele; F – perovszkitot tartalmazó szimplektit közeli felvétele. A rövidítések Whitney és Evans (2010) alapján, továbbá Zrc – cirkonolit.*

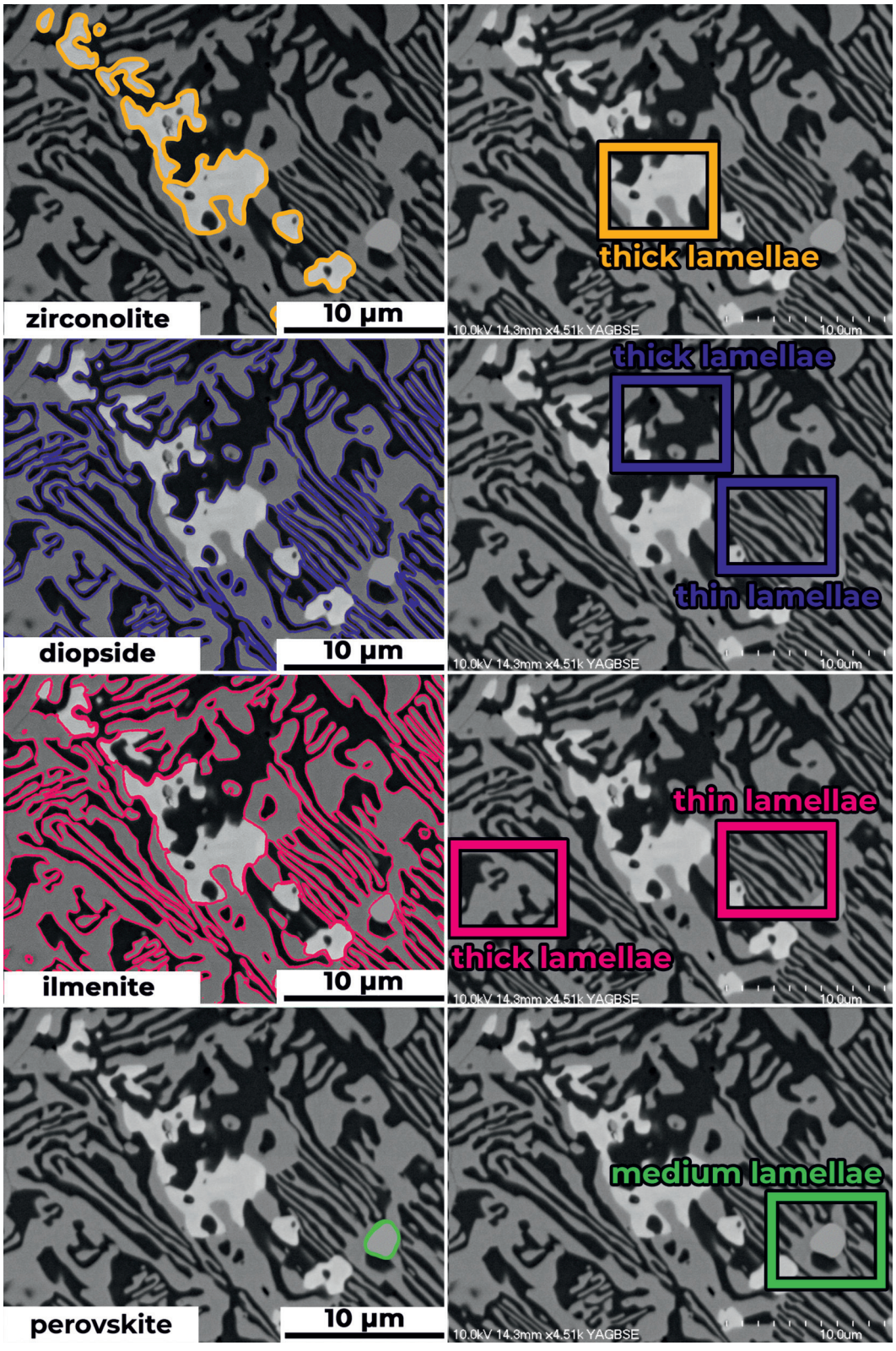

Figure 3. Representative BSE images of symplectites, Oldoinyo Lengai, Tanzania. Symplectites show white zirconolite lamellae with orange outlines, dark grey diopside lamellae with blue outlines, light grey ilmenite lamellae with pink outlines, and grey REE-perovskite lamellae with green outlines. Thick lamellae stand for coarse-grained lamellae, while thin lamellae stand for fine-grained lamellae.

3. ábra. *Reprezentatív, BSE-módban készült képek a szimplektitekről (Oldoinyo Lengai, Tanzánia). A narancssárgával körberajzolt részek a szimplektitek cirkonolitját mutatják; a kékkel körvonalazott részek a diopszid alkotót; a rózsaszínnel körbevett részek az ilmenitet jelzik; a zölddel körberajzolt rész pedig a RFF-perovszkitot mutatja. A „thick" (vastag) lamella a durvaszemcsés lamellákra utal, míg a „thin" (vékony) lamella a finomszemcsésekre.*

corroded margins. The zones of groundmass clinopyroxene ranges from diopside (light green, mg# =86–98) to aegirine-augite (dark green, mg# = 58–80). The diopside zones are rich in fine-grained (50 μm) euhedral inclusions of magnetite and perovskite, whereas the aegirine-augite zones host inclusions of titanite. Both zones host randomly distributed primary melt inclusions also. Nepheline is euhedral, homogeneous in composition, and hosts randomly distributed clinopyroxene and melt inclusions. Titanite occurs in two forms: 1/ large (~1 mm) subhedral crystals with magnetite and perovskite inclusions; 2/ anhedral crystals with fewer or no mineral inclusions. The latter usually occurs close to the double coronas. All titanites are homogeneous in composition and contain small amounts of ZrO_2 (0.4–0.8 wt%).

The groundmass contains large oriented and euhedral light brown phlogopite phenocrysts (mg# = 81–85) containing magnetite, perovskite, apatite, diopside and primary melt inclusions. The phenocrysts commonly exhibit kink bands. All phlogopites have dark brown anhedral rims of biotite (mg# =55–61).

The double coronas surround a large, up to 2 mm, olivine xenocrysts in the center (mg# = 80–83) with a corroded rim. Olivine is interpreted as a xenocryst, as indicated by its corroded margins and the development of reaction coronas, reflecting disequilibrium with the host magma and incorporation from an earlier, compositionally distinct mantle-derived assemblage (see details in Halász et al. 2023). The olivine is surrounded by a fine-to-medium sized (<0.05 and 0.05–2 mm) inner clinopyroxene corona (diopside with mg# = 88–98, to augite with mg# ~78), and an outer mica corona (mg# = 83–85) (*Fig. 2b*). Clinopyroxene and phlogopite corona host randomly distributed (primary) melt inclusions and mineral inclusions of magnetite, perovskite, and also tiny symplectic microtextures (hereafter referred to as symplectite) in some cases (*Fig. 2c,d*).

Minerals of the symplectites

The symplectites vary between 50 and 180 μm in diameter and are opaque in transmitted light optical microscope (*Fig. 2c*). Nevertheless, backscattered electron images (BSE) (*Fig. 2d*) reveal that symplectite texture consists of a complicated interfingering of three types of lamellae: wavy bright white (zirconolite), light grey (ilmenite) dark grey (diopside) (*Fig. 2e*, *Fig. 3*); and in some symplectites a pale white lamella type also occurs (REE-bearing perovskite) (*Fig. 2f*). The lamella thickness shows a bimodal distribution in the case of diopside and ilmenite that appear as both coarse-grained and fine-grained lamellae (*Fig. 3*), while zirconolite forms solely coarse-grained lamellae (*Fig. 2f* and *Fig. 3*) and REE-bearing perovskite forms a few medium-grained lamellae.

Diopside

As mentioned above, diopside in symplectites appears as both coarse-grained and fine-grained lamellae. It shows no chemical zonation and is pure diopside with mg# of 86–96 (Fe^{II} 0.03–0.09, Fe^{III} 0.10–0.12, Mg 0.81–0.85, Na 0.03–0.09 apfu) (see *Table I* in the Electronic Supplementary Materials – ESM). As diopside occurs ubiquitously in the groundmass, in the double coronas, and in the symplectites, it is possible to make correlation (see details in the Discussion).

Ilmenite

Despite the geometry of the lamellae, both coarse-grained and fine-grained ilmenite lamellae contain (all in wt%) 40.2–40.9 FeO^T, 50.3–50.7 TiO_2, 1.7–2.0 MnO, 5.7–6.2 MgO, 0.2 CaO, 0.1–0.3 Al_2O_3 (see *Table 2.* in ESM). The studied phase in the ilmenite-geikilite-pyrophanite solid solution is closest to the ilmenite component (75.6-77.6 % apfu), with a slight geikilite component (19.2-20.8 % apfu) and negligible pyrophanite component (3.2-3.8 % apfu) based on the mineral formula.

Perovskite

The perovskite of the symplectites forms medium sized lamellae, and is enriched in FeO^T, Nb_2O_5, ZrO_2, HfO_2, SrO or REE (see *Table II.* in ESM). Based on the nomenclature triangle, they are shifted from the ideal ($CaTiO_3$) perovskite composition toward the loparite and lueshite components but are still perovskite (Mitchell & Valdykin 1993, Mitchell 2002) (*Fig. 4*). Besides the symplectites, perovskite appears in the groundmass minerals as inclusions (see correlation in Discussion).

Zirconolite

Zirconolite appears only in the symplectites as coarse-grained lamellae and contains (all in wt%) CaO (18.3–21.0), ZrO_2 (18.1–22.3), TiO_2 (42.6–47.6), FeO^T (4.2–7.2), MgO (1.3–1.6), Al_2O_3 (0.3–1.3) and is enriched in ThO_2 (0.2–0.8), UO_2 (0.1–0.6), and LREE (0.2–0.8), Y_2O_3 (0.2–0.9) (*Table I*). STEM-EDS map shows zonation of zirconolite (*Fig. 5*),

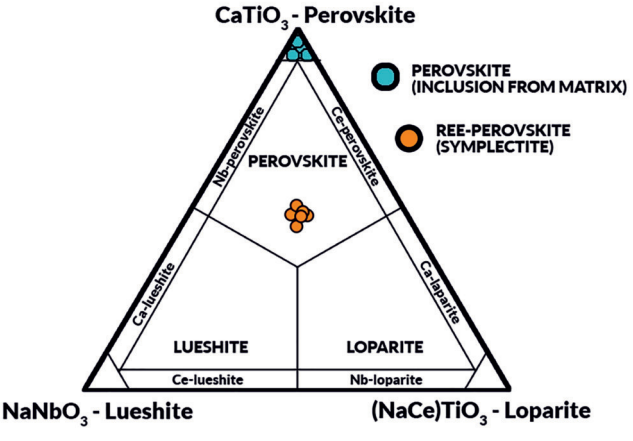

Figure 4. Compositions of REE-bearing perovskite from symplectites, and the perovskite inclusions from the groundmass clinopyroxenes, Oldoinyo Lengai micro-ijolite, Tanzania. The figure contains the modified diagrams of Mitchell & Valdykin (1993), Mitchell (2002).

4. ábra. *Az Oldoinyo Lengairól származó olivin-flogopit mikro-ijolit mintákból származó perovszkitok összetételét mutató háromszögdiagram. A narancssárga körök a szimplektitekben található RFF-perovszkitot, a kék körök pedig az olivin-flogopit mikro-ijolit alapanyagában lévő klinopiroxének perovszkitzárványait mutatják. Az ábra Mitchell és Valdykin (1993) és Mitchell (2002) után módosítva.*

Table I. Main element oxide contents in selected zirconolite grains from Oldoinyo Lengai micro-ijolite, Tanzania, in weight percent by EDS (normalized). FeOT represents total iron oxide content. Each measurement from number 1 to 6 stands for different grains; 7 is an area measurement from the interior of a zoned zirconolite grain, while measurements 8 and 9 represent the core and rim analyses from the same zoned grain based on the element map. The measured lead values may be uncertain due to the properties of the sample mount; however, since lead is present in several zirconolite grains, its presence cannot be ruled out based on the measurement, although it should be interpreted with caution. Based on the instrument and the different types of measurements, the LLD value is generally in the range of about 0.1–0.5 wt% for EDS analyses.

I. táblázat. *Néhány reprezentatív cirkonolitszemcse főelem összetétele (tömegszázalékban) oxidos formában a Oldoinyo Lengai (Tanzánia) mikro-ijolitjából, EDS-analízis alapján (normálva). A FeOT a teljes vas-oxid-tartalmat jelöli. Az 1-től 6-ig számozott mérések különböző szemcsékre vonatkoznak; a 7-es egy zónás cirkonolitszemcse belső részéből származó területi mérés, míg a 8-as és 9-es mérések ugyanazon zónás szemcse mag- és peremösszetételét reprezentálják. A mért ólomértékek bizonytalanok lehetnek a mintatartó tulajdonságai miatt; ugyanakkor mivel több cirkonolitszemcsében is kimutatható az ólom jelenléte, a mérések alapján nem zárható ki az ásvány ólomtartalma sem, de az eredményeket óvatosan kell értelmezni. A műszer és a különböző mérési módszerek alapján az EDS-analízisekre jellemző LLD (kimutatási határ) értéke általában körülbelül 0,1–0,5 tömegszázalék.*

	EDS						TEM		
	main element oxide contents in weight percent (wt%)								
	1	**2**	**3**	**4**	**5**	**6**	**7**	**8**	**9**
SiO_2	1.5	1.3	2.3	1.2	2.9	1.8	1.7	3.2	2.4
TiO_2	43.0	42.6	44.0	44.7	44.6	44.9	47.1	43.6	47.6
$Al2O_3$	0.5	0.9	0.6	0.3	1.1	0.5	1.2	1.2	1.3
FeO^T	7.0	6.7	6.8	6.9	6.6	7.1	4.4	7.0	4.2
MgO	1.3	1.4	1.6	1.3	2.7	1.2	n.d.	n.d.	n.d.
CaO	19.1	18.7	18.5	19.3	19.0	18.3	21.0	19.7	21.1
Nb_2O_5	3.5	3.6	3.5	3.6	2.9	2.9	2.1	3.0	2.0
Ce_2O_3	n.d.	n.d.	n.d.	n.d.	0.9	0.8	0.3	0.6	0.4
UO_2	0.4	0.5	0.3	0.4	0.3	0.3	0.1	0.6	0.1
ThO_2	0.7	0.5	0.5	0.5	0.4	0.6	0.2	0.8	0.2
ZrO_2	22.1	22.3	20.5	20.6	18.1	21.5	20.9	19.5	19.6
Nd_2O_3	n.d.	0.7	0.7	n.d.	n.d.	n.d.	0.2	0.3	0.2
Y_2O_3	0.7	0.5	0.5	0.9	0.4	0.2	0.8	0.5	0.8
PbO	n.d.	n.d.	n.d.	n.d.	n.d.	n.d.	n.d.	0.1	0.1
Ta_2O_3	0.1	0.3	0.1	0.3	0.3	n.d.	n.d.	n.d.	n.d.
analytical sum	100.0	100.0	100.0	100.0	100.0	100.0	100.0	100.0	100.0
	numbers of cations based on 4 O in atoms per formula unit (apfu)								
Si	0.09	0.08	0.13	0.07	0.19	0.10	0.09	0.18	0.13
Ti	1.83	1.82	1.85	1.90	1.83	1.89	1.95	1.83	1.97
Al	0.04	0.06	0.04	0.02	0.07	0.03	0.08	0.08	0.08
Fe^{II}	0.29	0.28	0.29	0.30	0.28	0.31	0.19	0.31	0.18
Fe^{III}	0.04	0.04	0.03	0.03	0.02	0.02	0.01	0.02	0.01
Mg	0.11	0.11	0.13	0.11	0.22	0.11	–	–	–
Ca	1.16	1.14	1.11	1.17	1.11	1.10	1.24	1.18	1.24
Nb	0.09	0.09	0.09	0.09	0.07	0.07	0.05	0.08	0.05
Ce	–	–	–	–	0.02	0.02	0.01	0.01	0.01
U	0.00	0.01	0.00	0.01	0.00	0.00	0.00	0.01	0.00
Th	0.01	0.01	0.01	0.01	0.01	0.01	0.00	0.01	0.00
Zr	0.61	0.62	0.56	0.57	0.48	0.59	0.56	0.53	0.53
Nd	–	0.01	0.01	–	–	–	0.00	0.01	0.00
Y	0.02	0.02	0.01	0.03	0.02	0.01	0.02	0.01	0.02
Pb	–	–	–	–	–	–	–	0.00	0.00
Ta	0.00	0.00	0.00	0.00	0.00	–	–	–	–
sum cations	4.07	4.08	4.13	4.10	4.08	4.07	4.22	4.26	4.23

although the STEM-EDS alone, neither proves nor rules out the presence of non-zoned grains. The SEM analyses (*Fig. 8b*), however, demonstrate that there are presumably zirconolite grains in both zoned and non-zoned varieties. This assumption is also supported, though not conclusively proven, by the STEM-EDS data. In the zoned grains, there is extreme zonation in U, Th, and Fe, and slight zonation is present in most trace elements. Thorium is also enriched in the U-rich zones, while Nd, Nb and Ce are slightly increased (*Fig. 5*). There is no difference in the content of Zr, Y in the U-rich and U-poor zones. In the zoned grains, the enrichment of U, Th, Fe, Nd, Nb, and Ce increases towards the rims (*Fig. 5*).

Symplectites were also examined at nanoscale to understand the crystal type and chemical composition of zirconolite. High-resolution STEM-HAADF images and SAED patterns are consistent with the same monoclinic crystal structure, suggesting that the studied zirconolite belongs to the zirconolite-2M polytype. In addition, the images reveal a characteristic twinning pattern (*Fig. 6*), where each zirconolite crystal is built by two twin domains (X and Y) of variable thicknesses. The twin relationship was studied in two orientations (α and β) of the crystals (by tilting the sample ~30° around [001]), displaying two pairs of orientations. In orientation α, the [1-10] and [010] and in orientation β, the [100] and [130] zone axes are parallel to the electron beam and belong to X and Y twin domains, respectively (*Fig. 7*). Although this orientation relationship between twin domains looks similar to that described by WHITE et al. (1984), we found the twin axis to be parallel to [110] (resulting in 180° rotation around the [110], with the contact plane parallel to (001)). For visualization, see the Supplementary info. The density of twin boundaries changes across the studied zirconolite crystals (*Fig. 6a*); however, within the limits of the STEM-EDS technique, no compositional differences were associated with the varying density of defects.

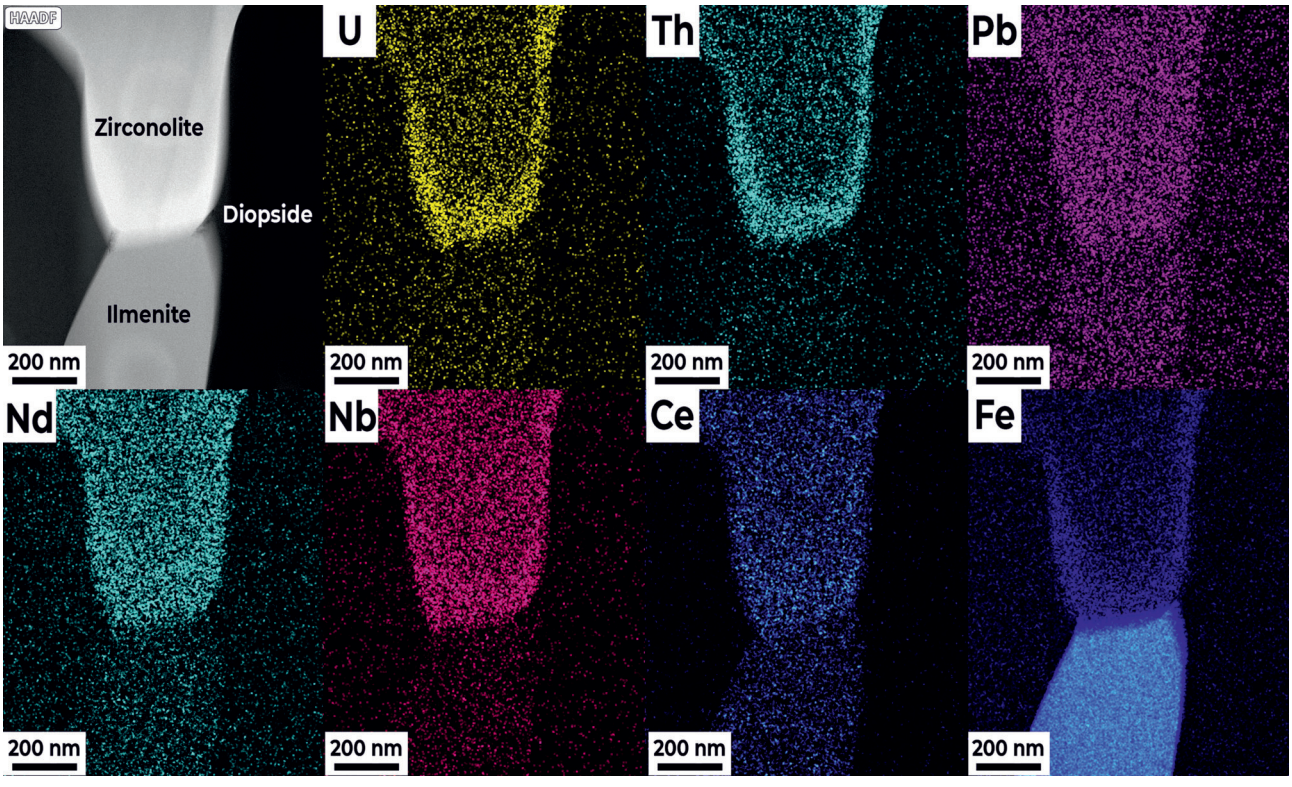

Figure 5. STEM HAADF image and STEM-EDS element maps of a zoned zirconolite grain, Oldoinyo Lengai micro-ijolite, Tanzania. The changes in colour intensities are related to the concentration changes of the indicated elements. The intensity of colours were calculated from the "net" peak intensities, which are integrated from EDS spectra after background correction and peak deconvolution. The colour intensities are normalized for the better visualization. The low Pb content on the element map may originate from both the sample and the sample holder, therefore its interpretation is uncertain.

5. ábra. *STEM HAADF-kép és STEM-EDS-elemtérképek egy az Oldoinyo Lengai (Tanzánia) olivin-flogopit mikro-ijolitjából származó, zónás cirkonolitszemcséről. A színeken belüli intenzitás az elemek koncentrációváltozását mutatja. A színintenzitások a „net peak" intenzitások alapján kalkuláltak az EDS-spektrumokból. A jobb vizualizáció érdekében a színintenzitások normalizáltak. Az elemtérképen megfigyelhető alacsony Pb-tartalom származhat magából a mintából, de a mintatartóból is, ezért értelmezése bizonytalan.*

Discussion

Evolutionary overview for olivine-phlogopite micro-ijolite enclaves

This section provides a brief summary of the previously established petrogenetic framework of olivine-phlogopite micro-ijolites (Halász et al. 2023), in order to place the present study's observations into context.

Olivine-phlogopite micro-ijolites are heterogeneous and compositionally complex rocks that contain a mixture of minerals crystallized at different stages during the evolution of an olivine-nephelinite parental magma, as a result of multiple magma injections (for details, see Halász et al. 2023, fig. 9). During this process, two distinct parageneses developed, alternating several times throughout crystallization: the "diopside paragenesis" at 970–1070 °C and the "aegirine-augite paragenesis" at 700–850 °C (Halász et al. 2023). The formation of diopside and nepheline together with their subordinate magnetite and perovskite inclusions, occurred during the "diopside paragenesis"; whereas aegirine-augite and titanite formed during the "aegirine-augite paragenesis". The alternating zonation is interpreted to have developed from repeated injections of hot magma followed by cooling periods. This hypothesis is supported by the occurrence of anhedral titanite in the groundmass, interpreted as resorbed titanite formed during renewed magma influx. The observed ductile deformation of the phlogopite phenocrysts further supports this interpretation.

The olivine of the double coronas represents an early magmatic liquidus phase from a silicate melt of metasomatized mantle origin. As the magmatic environment evolved, the olivine became unstable, leading to its partial dissolution and the formation of a corroded rim. Clinopyroxene coronas around olivine in the Oldoinyo Lengai system are generally interpreted as reaction products of the olivine and a nephelinitic magma (Dawson et al. 1995, Sekisova et al. 2015). However, the presence of randomly distributed primary melt inclusions, whose compositions are similar to those of groundmass clinopyroxenes, indicates a magmatic origin. The clinopyroxene corona grew on the olivine using it as a nucleus, while the outer mica corona is interpreted to have formed as a result of magmatic dynamics.

All the constituents mentioned above in the olivine-phlogopite micro-ijolites are of magmatic origin, except for the symplectites of the double coronas, which are interpreted here as having formed through subsolidus processes during magmatic evolution. Alternative interpretations are discussed below, while the broader crystallization framework of the host rocks has been established in detail by Halász et al. (2023).

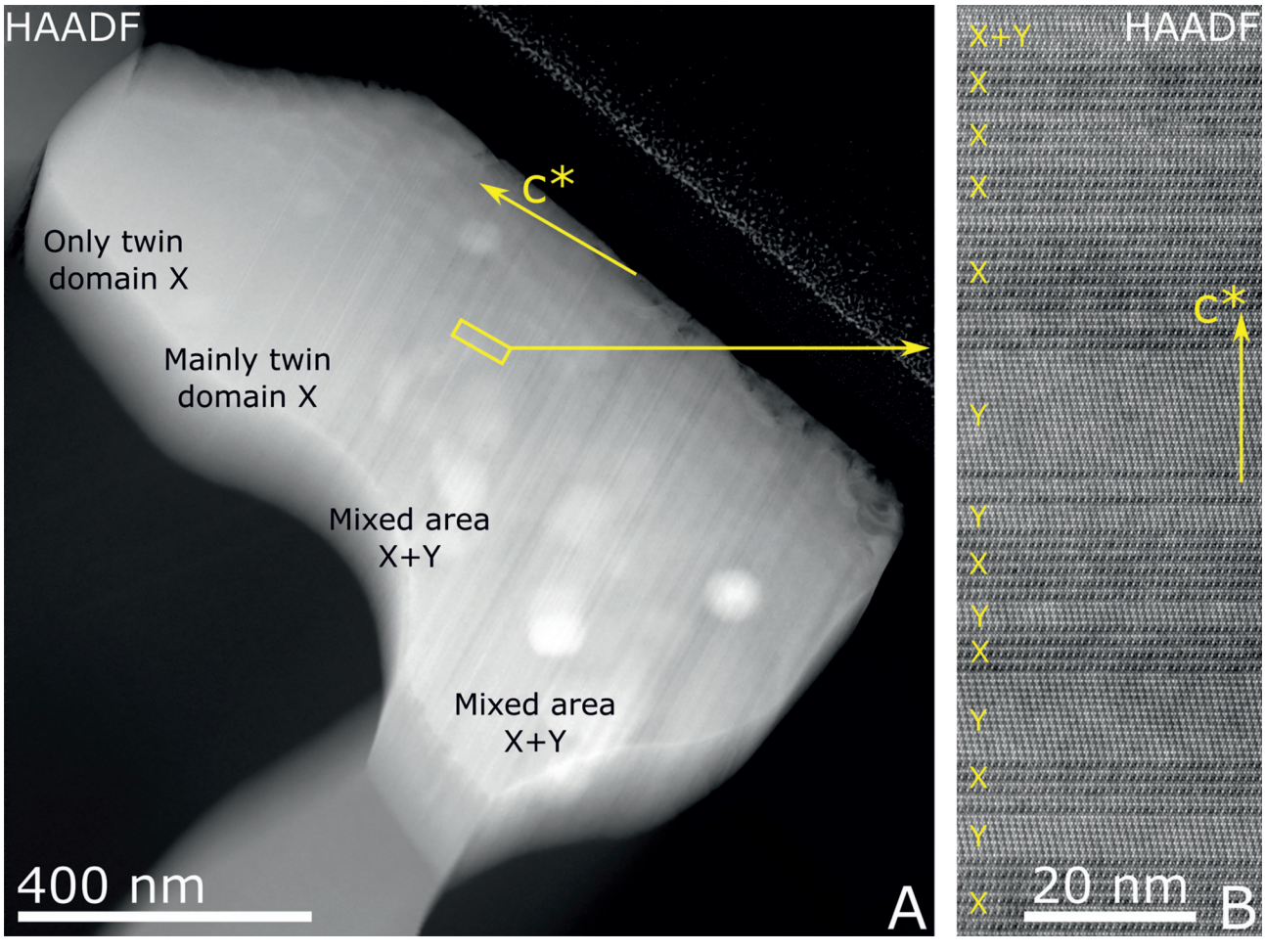

Figure 6. Visualisation of twinning in a zirconolite crystal, Oldoinyo Lengai micro-ijolite, Tanzania. A – STEM HAADF image shows variation in the thicknesses of twin lamellae X and Y and a gradation in twin boundary density within the crystal; B – The alternation of X and Y twin lamellae can be observed in an atomic-resolution STEM HAADF image taken from the mixed area marked with a yellow rectangle in (A) (the image in (B) was rotated to align c* vertical).

6. ábra. *Az ikresedés megjelenése egy cirkonolitkristályban a Oldoinyo Lengai (Tanzánia) mikro-ijolitjából. A – STEM HAADF-kép, amely az X és Y ikerlemezek vastagságának változását, valamint az ikerhatár-sűrűség fokozatos változását mutatja a kristályon belül; B – az X és Y ikerlemezek váltakozása megfigyelhető egy atomi felbontású STEM HAADF-képen, amely az (A) ábrán sárga téglalappal jelölt kevert területen készült. A B ábrarészen látható kép úgy készült, hogy azt elforgatták úgy, hogy a c* irány függőleges legyen.*

Solid-solid reaction

Usually, symplectite textures develop as reaction products or as solid-state mineral reactions due to slow grain-boundary diffusion relative to interface propagation rate (HIROI et al. 1997, OBATA 2011, GAIDIES et al. 2017). Alternatively, it may be induced by changes in pressure, temperature or fluid composition by oxidation or dehydrogenation (GAIDIES et al. 2017). Considering the evolution of the host olivin-phlogopite micro-ijolites and the properties of the symplectites in the studied samples, the most likely formation mechanism is a solid-phase reaction, facilitated by changes in temperature.

Two minerals could have triggered this solid phase reaction: the early-stage magmatic olivine (T >1 100 °C) and later-stage magmatic titanite (700–780 °C). These minerals cannot coexist under equilibrium due to their stabilities at different silica activity (CARMICHAEL et al. 1970). This is consistent with experimental and thermodynamic studies that have extensively explored titanite stability under varying temperature–fO_2–$aSiO_2$ conditions (XIROUCHAKIS et al. 2001a,b), which demonstrate that olivine + titanite assemblages are only stable within a narrow range of silica activity and redox conditions, and are otherwise prone to react to form diopside + ilmenite.

During the progressive crystallization of olivine-phlogopite micro-ijolite, titanite and olivine were in close proximity within the double coronas, allowing the following reaction to occur:

$$(Fe,Mg)_2SiO_4 + CaTiSiO_5 \rightarrow FeTiO_3 + CaMgSi_2O_6 \quad (1)$$

olivine + titanite → ilmenite + diopside

Equation 1 is a typical example of a solid–solid reaction commonly observed in metamorphic settings (VERNON 2004), but rarely documented during active magmatic crystallization. The presence of such symplectites provides clear evidence for simultaneous subsolidus processes occurring during ongoing magmatic crystallization. The reaction above

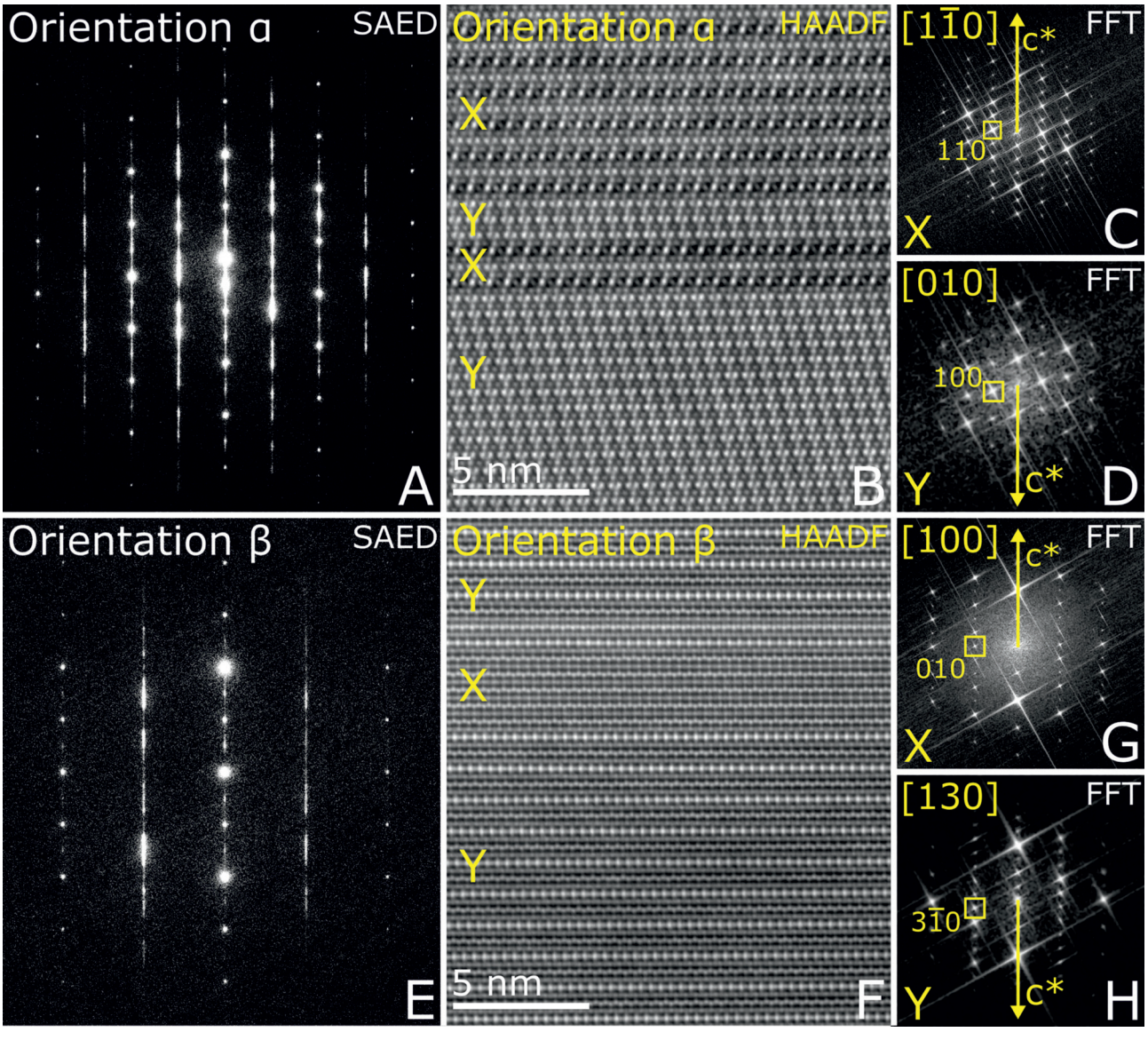

Figure 7. Determination of twinning conditions in zirconolite by evaluating two crystal orientations (α and β) of the same crystal at ~30° from each other, Oldoinyo Lengai micro-ijolite, Tanzania. A – SAED pattern of a twinned zirconolite crystal displayed in *Fig. 4*, in orientation α, composed of the diffraction patterns produced by domains X and Y; B – atomic-resolution STEM HAADF micrograph obtained in orientation α, displaying both X and Y twin domains; C – fast-Fourier transform (FFT) of an area containing only the X twin domain, consistent with [1-10] being parallel to the electron beam; D – FFT of an area containing only the Y twin domain, consistent with [010] being parallel to the electron beam; E – SAED pattern of a twinned zirconolite in orientation β; F ¬– atomic-resolution STEM HAADF micrograph obtained in orientation β, displaying both X and Y twin domains; G – FFT of an area containing only the X twin domain, consistent with [010] being parallel to the electron beam; H – FFT of an area containing only the Y twin domain, consistent with [130] being parallel to the electron beam. (The FFTs in C, D, G, and H do not correspond to the exact areas displayed in images B and F but to larger areas of the same crystal that contain either X or Y domains.)

*7. **ábra.** Az Oldoinyo Lengai (Tanzánia) olivin-flogopit mikro-ijolitjából származó cirkonolit ikresedési feltételeinek meghatározásához ugyanazon kristály ~30°-kal elforgatott két kristályorientációja (α és β) látható az A és E képeken. A – a* 4. ábrán *bemutatott ikres cirkonolitkristály SAED-diffrakciós képe α orientációban, amely az X és Y domének által létrehozott diffrakciós mintázatokból tevődik össze; B – α orientációban készült, atomi felbontású STEM HAADF-mikrográfia, amely mind az X, mind az Y ikerdoméneket mutatja; C – kizárólag az X ikerdomént tartalmazó terület gyors Fourier-transzformációja (FFT), ahol az [1-10] irány párhuzamos az elektronsugárral; D – kizárólag az Y ikerdomént tartalmazó terület FFT-je, ahol a [010] irány párhuzamos az elektronsugárral; E – a* 4. ábrán *bemutatott ikres cirkonolit kristály SAED-diffrakciós képe β orientációban; F – β orientációban készült, atomi felbontású STEM HAADF-mikrográfia, amely mind az X, mind az Y ikerdoméneket mutatja; G – kizárólag az X ikerdomént tartalmazó terület FFT-je, ahol a [010] irány párhuzamos az elektronsugárral; H – kizárólag az Y ikerdomént tartalmazó terület FFT-je, ahol az [130] irány párhuzamos az elektronsugárral. (A C, D, G és H ábrákon bemutatott FFT-k nem pontosan a B és F képeken látható területeknek felelnek meg, hanem ugyanazon kristály nagyobb kiterjedésű részeinek, amelyek kizárólag X vagy Y doméneket tartalmaznak.)*

confirms that ilmenite and diopside are reaction products. Ilmenite is purely a reaction product as it only occurs in the symplectites not elsewhere in the host rocks. While ilmenite is rare in Oldoinyo Lengai rocks, is not unique appearing in olivine-free rocks (Dawson 2008, Carmody 2012, Sekisova et al. 2015). In contrast, diopside occurs in the groundmass, in the double coronas, and also in the symplectites, which allows for a correlation. While the groundmass and corona clinopyroxenes are built by different zones, the diopside of the symplectites shows no chemical zonation, however, its

composition closely resembles the diopside zone of the groundmass clinopyroxenes. Such diopsides are very common in the Oldoinyo Lengai plutonic rocks (i.e., ijolite, pyroxenite, jacupirangite, and olivine-mica ijolite) either as solely crystals or as zones (DAWSON & SMITH 1992; DAWSON et al. 1995, 2008; CARMODY 2012; SEKISOVA et al. 2015; HALÁSZ et al. 2023).

While equation-1 confirms that ilmenite and diopside are reaction products; it does not explain the presence of zirconolite and REE-perovskite. As perovskite is a typical early-stage accessory phase in many silica-undersaturated igneous rocks and non-silicate rocks such as carbonatites and oxide cumulates (VEKSLER & TEPTELEV 1990, BERKESI et al. 2023), it is common in Oldoinyo Lengai rocks, also appear in the olivine-phlogopite micro-ijolite as inclusion. These inclusion perovskites are not enriched in FeO^T, Nb_2O_5, ZrO_2, HfO_2, SrO or REE (see HALÁSZ et al. 2023), and they plot as ideal ($CaTiO_3$) perovskites (MITCHELL & VALDYKIN 1993, MITCHELL 2002) (*Fig. 4*). In contrast the REE-bearing perovskites of the symplectites are enriched in those elements (see *Table II.* in Supplementary info) and deviate from ideal compositions toward lueshite- and loparite-like components (*Fig. 4*). These two perovskite populations (1/ REE-bearing symplectite ones, 2/ inclusion ones) are genetically unrelated, as evidenced by the reasons mentioned above.

Zirconolite occurs exclusively in the symplectites, precluding direct, within-sample petrographic correlation. However, it is possible to correlate it to other zirconolites. Based on the Ca-Zr-Ti diagram of GIERÉ et al. (1998), the studied zirconolites are close to nominal composition ($(Ca,Y)Zr(Ti,Mg,Al)_2O_7$), slightly shifted to the metasomatic and carbonatite zirconolites (*Fig. 8a*). As the zirconolite contains ACT and REE elements, the diagram of HURAI et al. (2018) (*Fig. 8b*) can further clarify its properties. Our unzoned zirconolites and the rims of the zoned zirconolite crystals overlap with those representing carbonatite and metasomatic rocks (*Fig. 8b*). The cores of the zoned grains overlap with the typical zirconolites of carbonatite and syenite, nephelinite systems. Zirconolites in metasomatically altered rocks typically exhibit a considerable variation of ACT and are generally relatively poor in Nb and Ta, while they are HREE (Y) dominated (GIERÉ et al. 1998). None of these characteristics are typical to the zirconolites we studied. Concurrently, the zirconolites from carbonatite rocks are rich in Nb, their FeO^T content is higher than their MgO content, and their LREE (La, Ce, Nd) content is higher compared to their HREE (Y) content (GIERÉ et al. 1998). This is similar to our studied samples. The amount of ACT and REE may help to understand the crystallization conditions and give a possible explanation for the twinning characteristics of the studied zirconolites. Increasing ACT and REE tend to produce twinning in zirconolite (VANCE et al. 1994, COELHO et al. 1997, BEGG & VANCE 1997), a property also found in out studied zirconolite grains. While diopside and perovskite regularly appear in Oldoinyo Lengai rocks, and ilmenite is also not unique, zirconolite has not been documented yet.

Zirconolite likely did not form directly via the olivine + titanite reaction but rather crystallized from contemporaneous magmatic processes. Nevertheless, the breakdown of titanite during the solid-state reaction released Zr (0.4–0.8 wt%), which contributed to zirconolite crystallization. Zirconolite can be primary magmatic mineral in carbonatite systems, as it was found in melt inclusions from Kerimasi (KÁLDOS et al. 2015). The mineral chemistry of zirconolite indicates formation during the late stages of magmatic evolution in a REE-enriched environment, consistent with co-crystallization of REE-perovskite (MITCHELL 2002). While the nearly ideal CaTiO perovskite inclusions formed at high temperatures during the "diopside paragenesis" (970–

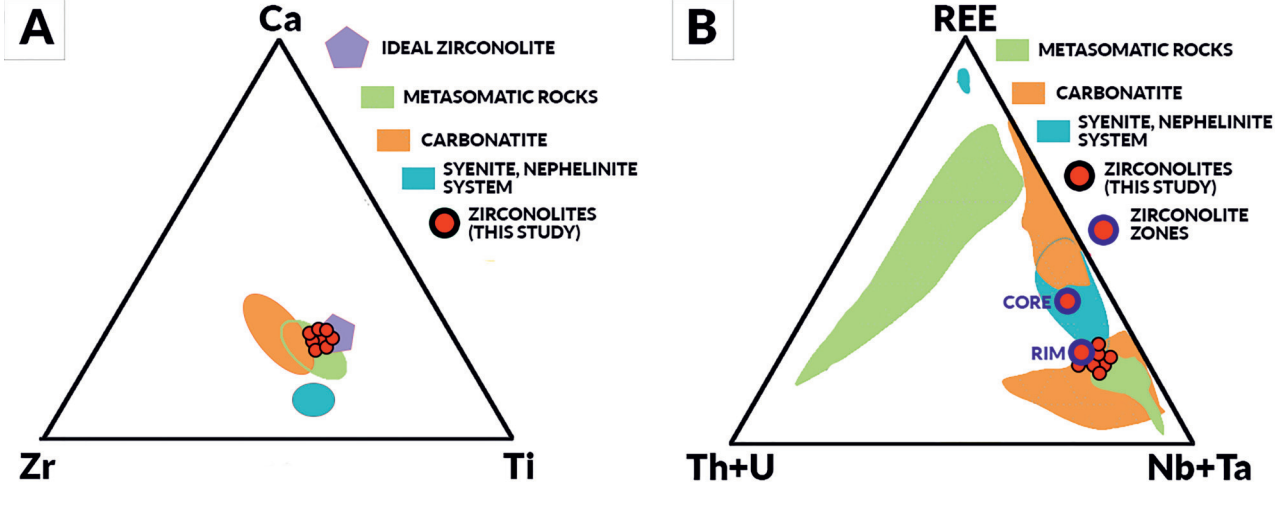

Figure 8. Compositions of zirconolite from distinct petrographic settings, Oldoinyo Lengai micro-ijolite, Tanzania. The figure contains the modified diagrams of GIERÉ et al. (1998) and HURAI et al. (2018). The plots of our samples on both A and B Figure are based on 15 analyses (n=15). The core and rim plots on Figure B show the results of TEM measurements.

8. ábra. *Az Oldoinyo Lengai (Tanzánia) mikro-ijolitjából származó cirkonolit összevetése különböző petrográfiai tulajdonságokkal rendelkező más cirkonolitszemcsékkel. Az ábra GIÉRE et al. (1998) és HURAI et al. (2018) után módosítva. Az A és B ábrákon található saját mérések 15 analízisre alapulnak (n=15). A mag-szegély (core-rim) jelek a B ábrán a TEM-mérések adatait mutatják.*

1070 °C), the REE-bearing perovskites of the symplectites likely crystallized at lower temperatures, in later stages. Also, we cannot rule out the effect of a possible fluid phase, as it is known that REE can be transported in carbonatite fluids (Mororó et al. 2024, Yuan et al. 2024), however based on the composition and *Figure 8* it is not likely. Ideally, the U, Th content and the lack of common lead, makes zirconolite a potential U–Pb chronometer (Lumpkin et al. 1994, Williams & Gieré 1996, Rasmussen & Fletcher 2004, Hurai et al. 2018, Wang et al. 2021), however, the size of the studied zirconolite grains is too small, and number of the grains is also quite low, not making possible a reliable calculation for the age of this mineral.

Temperature change and symplectite grain sizes

The crystal size distribution of the symplectites is bimodal: diopside and ilmenite form both coarse-grained (2–3 μm) and fine-grained (<2 μm) lamellae, while zirconolite shows solely coarse-grained (~5 μm) lamellae, and REE-perovskite form medium-size lamellae (*Fig. 2f*, *Fig. 3*). Typically, low-temperatures crystallization produces fine-grained lamellae, while high-temperature conditions promote the growths of coarse-grained lamella (Hoffmann & Weeks 1962, Weeks 1963, Marxsen et al. 2020). Furthermore, variations in reaction speed may influence lamella thickness (Gaidies et al. 2017). We propose that the temperature fluctuations during the alteration of "diopside parageneses" and "aegirine-augite parageneses" caused the observed bimodal crystal size distribution. Consequently, the fine-grained lamellae of ilmenite and diopside likely formed at lower temperatures during the "aegirine-augite paragenesis", while the coarse-grained lamellae of zirconolite, ilmenite and diopside developed during the "diopside paragenesis" at higher temperature (*Fig. 9, Fig. 10*). The medium-sized lamellae of REE-perovskite likely formed at intermediate temperatures between the two parageneses. To test this hypothesis, we selected two representative diopside-ilmenite pairs that co-crystallized as coarse-grained lamellae within the symplectites and used them for thermometry following the method of Bishop (1980), assuming a pressure of 1000 to 7000 bars (*Table II*). The method is based on the distribution of Fe^{2+} and Mg between clinopyroxene and ilmenite, a well-established geothermometric indicator in both igneous and metamorphic rocks. The thermometer is expressed by the following equation:

$$T(°C) = \frac{748+2745*\left[\frac{Mg}{Mg+Fe^{Fe2+}}\right]^{cpx} + 817*\left[2*\left[\frac{Fe^{2+}}{Mg+Fe^{Fe2+}}\right]^{ln}\right] + 0.0106\,P}{ln\ln K_D} - 273 \quad (2)$$

where,

$$K_D = \frac{(\frac{Mg}{Fe})^{Cpx}}{(\frac{Mg}{Fe})^{Ilm}}$$

The thermometer is insensitive to pressure, and the results indicate that the coarse-grained lamellae of diopside and ilmenite crystallized at 1028–1057 °C. These values overlap with the temperature range of the diopside paragenesis (970–1070 °C), confirming that the symplectites formed during the ongoing crystallization: coarse-grained lamellae (ilmenite, zirconolite, diopside) formed at relatively high temperatures during the "diopside parageneses"; fine-grained lamellae (ilmenite, diopside) at lower temperatures during the "aegirine-augite parageneses" (*Fig. 10*); and the medium-sized lamellae of REE-perovskite formed at intermediate temperatures between the two parageneses (*Fig. 9*).

Conclusions

Our study presents the first documented occurrence of zirconolite from Oldoinyo Lengai. The mineral occurs within ilmenite–diopside–zirconolite ± REE-perovskite symplectites hosted in olivine-phlogopite micro-ijolite enclaves.

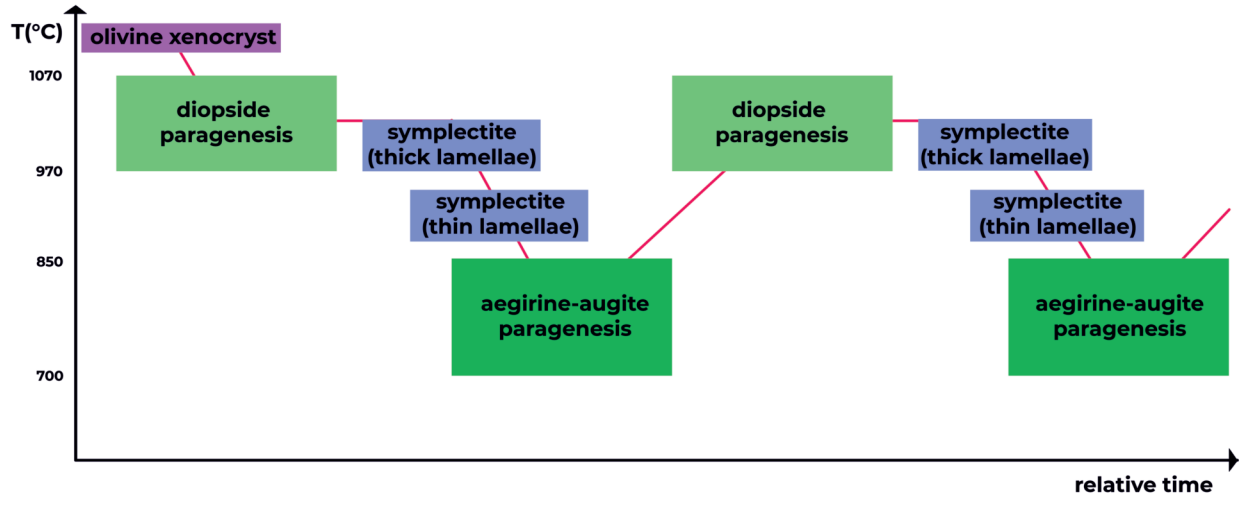

Figure 9. Schematic figure for the crystallisation of olivine-phlogopite micro-ijolite, Oldoinyo Lengai, Tanzania. The symplectites formed during crystallisation at different temperatures, probably in several steps. Thick lamellae stand for coarse-grained lamellae, while thin lamellae stand for fine-grained lamellae.

9. ábra. *Sematikus ábra az Oldoinyo Lengai olivin-flogopit mikro-ijolitok kristályosodási folyamatairól. A szimplektitek különböző hőmérsékleteken, feltehetőleg több lépésben keletkeztek. A „thick" vastag lamellák a durvaszemcsés lamellákra utalnak, míg a „thin" vékony lamella a finomszemcsésre.*

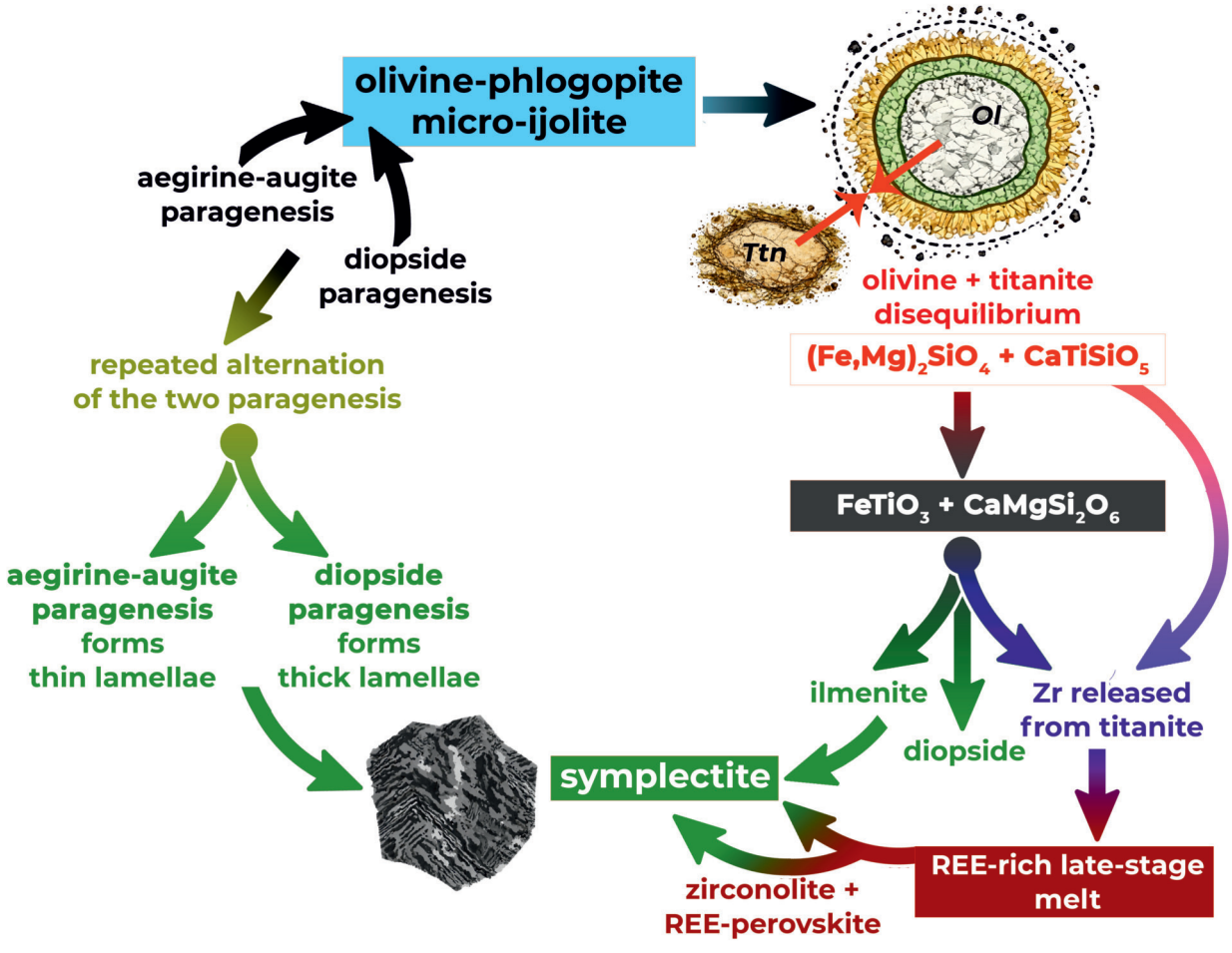

Figure 10. Schematic model of zirconolite-bearing symplectite formation in olivine–phlogopite micro-ijolite enclaves. Symplectites formed by a subsolidus reaction between olivine and titanite under disequilibrium conditions, producing diopside and ilmenite. Zirconolite did not crystallize directly from this reaction but formed from a late-stage, REE-rich melt, partly supplied by Zr released during titanite breakdown. Alternating high-temperature diopside and lower temperature aegirine-augite parageneses controlled the bimodal lamella size distribution, with coarse lamellae forming at higher temperatures and fine lamellae at lower temperatures.

10. ábra. *Sematikus modell, mely az olivin-flogopit mikro-ijolitban megtalálható cirkonolittartalmú szimplektitek kialakulását mutatja. A szimplektitek az olivin és titanit közötti nemegyensúlyi helyzet során, szubszolidusz körülmények mellett képződtek. Az olivin és titanit reakciója okozta a diopszid és ilmenit létrejöttét; míg a cirkonolit részben a titanit szétesése során felszabaduló Zr miatt jött létre a kristályosodás kései fázisában egy addigra RFF-gazdagabbá váló olvadékból. A magasabb hőmérsékletű diopszid paragenezis és alacsonyabb hőmérsékletű egirin-augit paragenezis váltakozása vezetett a bimodális lamella méret eloszláshoz a szimplektiten belül. A vastag lamellák magasabb hőmérséklethez, a vékonyabb lamellák pedig alacsonyabb hőmérséklethez kapcsolódva jöttek létre.*

The host rocks are complex, containing minerals crystallized at multiple stages, predominantly following two parageneses: high-temperature (~1028–1057 °C) "diopside paragenesis" and low-temperature (~700–850 °C) "aegirine-augite paragenesis". The symplectites represent solid–solid reaction textures formed during ongoing magmatic crystallization, specifically resulting from disequilibrium between early-formed olivine and late-crystallized titanite (see *Fig. 10*). The alteration of "diopside paragenesis" and "aegirine-augite paragenesis" also influenced the growths of the symplectites (*Fig. 10*).

The zirconolite crystals exhibit near-ideal compositions and belong to the zirconolite-2M polytype, showing characteristic twinning. The twin axis is parallel to [110], resulting in 180° rotation around the [110], with the contact plane parallel to [001]. The presence of REE and ACT elements may have induced the twinning (GIERÉ et al. 1998). The zirconolites' enrichment in actinides (U, Th) and LREEs together with co-crystallized REE-rich perovskite, suggests crystallization from a later-stage, incompatible-element-enriched melt, in contrast to the other constituents of olivine-phlogopite micro-ijolite enclaves. This highlights the coexistence of subsolidus mineral reactions and magmatic processes within the same temporal and environmental framework.

Our findings demonstrate that metamorphic-style subsolidus reactions – typically considered post magmatic – can also occur in situ active magmatic evolution (*Fig. 10*). This challenges the conventional separation of igneous and metamorphic domains. Zirconolite, towing to its composition and potential for U–Pb geochronology, may serve as a valuable tool for constraining the thermal and temporal evolution of carbonatite-associated alkaline systems, provided that future work identifies larger grains in sufficient abundance. Such grains could also shed light on the age of the magmatic activities beneath the Oldoinyo Lengai volcano.

Table II. Two typical diopside-ilmenite pairs and thermometry cf. BISHOP (1980). The mineral compositions are in weight percent by EDS (normalized). The pairs occur as coarse-grained intergrown lamellae in symplectites. Calculated temperatures are virtually pressure-insensitive and suggest formation at 1028–1057 °C.

II. táblázat. *Két reprezentatív diopszid-ilmenit pár termometriája BISHOP (1980) módszerét használva. Az ásványösszetételek tömegszázalékban vannak megadva, EDS-mérés alapján, normálva. A párok vastag (durvaszemcsés) lamellaként jelennek meg a szimplektiten belül. A számolt hőmérsékleti értékek alapvetően nyomásra nem érzékenyek, és 1028-1057°C-os kialakulást adnak.*

	main element oxide contents in weight percent (wt%) (EDS)			
	pair 1		**pair 2**	
	Ilm	**Di**	**Ilm**	**Di**
SiO_2	0.9	54.7	0.9	54.6
CaO	0.2	19.5	0.2	20.4
FeO^T	34.1	2.3	34.2	2.4
Al_2O_3	0.6	0.8	0.6	0.8
MgO	11.3	21.8	11.2	21.0
TiO_2	53.0	0.9	53.0	0.8
analytical sum	100.0	100.0	100.0	100.0
	numbers of cations, for Di based on 6 O, for Ilm based on 4 O in atoms per formula unit (apfu)			
Si	0.02	1.96	0.02	1.96
Ca	0.01	0.75	0.01	0.79
Fe^{II}	0.67	0.07	0.67	0.07
Fe^{III}	0.01	0.00	0.00	0.00
Al	0.02	0.03	0.02	0.03
Mg	0.39	1.16	0.39	1.12
Ti	0.93	0.03	0.93	0.02
sum cations	2.06	4.00	2.05	3.99
	thermometry			
P (kbar)		**T (°C)**		
1		1027.6		1049.6
2		1027.7		1050.7
3		1028.2		1051.2
4		1030.7		1052.4
5		1033.8		1054.8
6		1037.0		1055.7
7		1040.1		1056.8
	Minimum	Maximum	Minimum	Maximum
	1027.6	1040.1	1049.6	1056.8

Acknowledgements

We thank Levente ILLÉS (Institute of Technical Physics and Materials Science, Budapest) for preparing the FIB lamella. We thank Mohammad Sahroz Mohammad Eiaz KHAN for his assistance in enhancing the language of the manuscript. This study was supported by project NKFIH (National Research, Development, and Innovation Office of Hungary) K-142855 to Tibor GUZMICS and Márta BERKESI. Márta BERKESI was additionally supported by MTA FI FluidsByDepth Momentum research grant (nr. LP 2022-2/2022).

Availability of data and materials

All data contributing to this study are provided within the manuscript and/or the supplementary information file.

ESM Table I. Main element oxide contents of selected clinopyroxenes from distinct textural settings, Oldoinyo Lengai micro-ijolite, Tanzania. mg# – Mg/(Mg+Fe2+)*100, molar. The results present measurements obtained by the WDS method. The incorporation of Al into the tetrahedral and octahedral sites followed a charge-balanced fill-up approach.

DM I. táblázat. *Néhány reprezentatív, különböző szövettani helyzetből származó klinopiroxénszemcse főelemösszetétele (tömegszázalékban) oxidos formában az Oldoinyo Lengai (Tanzánia) mikro-ijolitjából, WDS-analízis alapján. A moláris mg# Mg/(Mg+Fe2+)*100 alapján van számolva. Az Al tetraéderi és oktaéderi pozícióját töltésegyensúly alapján kalkuláltuk.*

ESM Table II. Main element oxide contents of selected ilmenite and perovskite, Oldoinyo Lengai micro-ijolite, Tanzania. The results present measurements obtained by the EDS method (normalized). Based on the instrument and the different types of measurements, the LLD value is generally in the range of about 0.1–0.5 wt% for EDS analyses.

DM II. táblázat. *Néhány reprezentatív ilmenit és perovszkitszemcse főelemösszetétele (tömegszázalékban) oxidos formában az Oldoinyo Lengai (Tanzánia) mikro-ijolitjából, EDS-analízis (normált) alapján. A műszer és a különböző mérési módszerek alapján az EDS-analízisekre jellemző LLD (kimutatási határ) értéke általában körülbelül 0,1–0,5 tömegszázalék.*

3D model in supplementary. 3D model for the visualisation of zirconolite twinning. The twin relationship was studied in two orientations (α and β) of the crystals (by tilting the sample ~30° around [001]), displaying two pairs of orientations. In orientation α, the [1-10] and [010] and in orientation β, the [100] and [130] zone axes are parallel to the electron beam and belong to X and Y twin domains, respectively. The twin axis is parallel to [110] (resulting in 180° rotation around the [110], with the contact plane parallel to (001)). To open the 3D model, use 3D-builder in Windows or the following website: https://gltf-viewer.donmccurdy.com/

3D modell. *3D modell a cirkonolit ikresedésének szemléltetésére. Az ikerkapcsolat a kristály két orientációjában (α és β) lett vizsgálva (a minta kb. 30°-kal elfordítását követően a [001] tengely körül), két orientációpárt mutatva. Részletesen a* 7. ábra *mutatja meg az ikresedési vizsgálatot. A 3D modell megnyitásához használható a Windows-os 3D-builder, vagy az alábbi weboldal:*

https://gltf-viewer.donmccurdy.com/

References – Irodalom

ANENBURG, M., MAVROGENES, J.A., FRIGO, C. & WALL, F. 2020: Rare earth element mobility in and around carbonatites controlled by sodium, potassium, and silica. – *Science Advances* **6,** 65–70. https://doi.org/10.1126/sciadv.abb6570

BAKER, B.H., WILLIAMS, L.A.J., MILLER, J.A. & FITCH, F.J. 1971: Sequence and geochronology of the Kenya Rift volcanic. – *Tectonophysics* **11,** 191–215. https://doi.org/10.1016/0040-1951(71)90030-8

BAYLISS, P., MAZZI, F., MUNNO, R. & WHITE, T.J. 1989: Mineral nomenclature zirconolite. – *Mineralogical Magazine* **53,** 565–569. https://doi.org/10.1180/minmag.1989.053.373.07

BEGG, B.D. & VANCE, E.R. 1997: The incorporation of cerium in zirconolite. – *Materials Research Society Symp Proc* **465,** 333. https://doi.org/10.1557/PROC-465-333

BELLATRECCIA, F., DELLA VENTURA, G., WILLIAMS, C.T., LUMPKIN, G.R., SMITH, K.L. & COLELLA, M. 2002: Non-metamict zirconolite polytypes from the feldspathoid-bearing alkalisyenitic ejecta of the Vico volcanic complex (Latium, Italy). – *European Journal of Mineralogy* **14,** 809–820. https://doi.org/10.1127/0935-1221/2002/0014-0809

BERKESI, M., MYOVELA, J.L., YAXLEY, G.M. & GUZMICS, T. 2023: Carbonatite formation in continental settings via high temperature–high pressure liquid immiscibility. – *Geochimica et Cosmochimica Acta* **349,** 41–54. https://doi.org/10.1016/j.gca.2023.03.027

BISHOP, F.C. 1980: The distribution of Fe^{2+} and Mg between coexisting ilmenite and pyroxene with applications to geothermometry. – *American Journal of Science* **280,** 46–77. https://doi.org/10.2475/AJS.280.1.46

BROWN, C. & GIRDLER, R.W. 1980: Interpretation of African gravity and its implication for the breakup of the continents. – *Journal of Geophysical Research* **85,** 6443–6455. https://doi.org/10.1029/JB085iB11p06443

CARMICHAEL, I.S.E., NICHOLLS, J. & SMITH, A.L. 1970: Silica activity in igneous rocks. – *American Mineralogist* **55**, 246–263.

CARMODY, L. 2012: *Geochemical characteristics of carbonatite-related volcanism and sub-volcanic metasomatism at Oldoinyo Lengai, Tanzania.* – PhD thesis, University College London, London/UK, 338 p.

COELHO, A.A., CHEARY, R.W. & SMITH, K.L. 1997: Analysis and Structural Determination of Nd-Substituted Zirconolite-4M. – *Journal of Solid State Chemistry* **129,** 346–359. https://doi.org/10.1006/jssc.1996.7263

CONTI, P., PISTIS, M., BERNARDINETTI, S., BARBAGLI, A., ZIRULIA, A., SERRI, L., COLONNA, T., GUASTALDI, E. & GHIGLIERI, G. 2021: Tectonic setting of the Kenya Rift in the Nakuru area, based on geophysical prospecting. – *Geosciences* **11,** 80. https://doi.org/10.3390/geosciences11020080

CORTI, G. 2012: Evolution and characteristics of continental rifting: analogue modeling-inspired view and comparison with examples from the East African Rift System. – *Tectonophysics* **522–523,** 1–33. https://doi.org/10.1016/j.tecto.2011.06.010

DAWSON, J.B. 2008: The Gregory Rift Valley and Neogene–Recent volcanoes in Northern Tanzania. – *Geol. Soc. London, Memoirs* **33,** 112 p. https://doi.org/10.1144/M33

DAWSON, J.B., SMITH, J.V. & STEELE, I.M. 1994: Trace-element distribution between coexisting perovskite, apatite and titanite from Oldoinyo Lengai, Tanzania. – *Chemical Geology* **117,** 285–290. https://doi.org/10.1016/0009-2541(94)90132-5

DAWSON, J.B., SMITH, J.V. & STEELE, I.M. 1995: Petrology and mineral chemistry of plutonic igneous xenoliths from the carbonatite volcano, Oldoinyo Lengai, Tanzania. – *Journal of Petrology* **36,** 797–826. https://doi.org/10.1093/petrology/36.3.797

DE HOOG, J.C.M. & VAN BERGEN, M.J. 1997: Notes on the chemical composition of zirconolite with thorutite inclusions from Walaweduwa, Sri Lanka. – *Mineralogical Magazine* **61,** 721–725. https://doi.org/10.1180/minmag.1997.061.408.13

DELLA VENTURA G., BELLATRECCIA, F. & WILLIAMS, C.T. 2000: Zirconolite with significant REEZrNb(Mn,Fe)O from a xenolith of the Laacher See eruptive center, Eifel volcanics, Germany. – *Canadian Mineralogist* **38,** 57–65. https://doi.org/10.2113/gscanmin.38.1.57

DONALDSON, C.H., DAWSON, J.B., KANARIS-SOTIRIOU, R., BATCHELOR, R.A. & WALSH, J.N. 1987: The silicate lavas of Oldoinyo Lengai, Tanzania. – *Neues Jahrbuch für Mineralogie, Abhandlungen* **156,** 247–279.

EBINGER, C.J. & SLEEP, N.H. 1998: Cenozoic magmatism throughout East-Africa resulting from impact of a single plume. – *Nature* **395,** 788–791. https://doi.org/10.1038/27417

GAIDIES, F., MILKE, R., HEINRICH, W. & ABART, R. 2017: Metamorphic mineral reactions: porphyroblast, corona and symplectite growth. – In: HEINRICH, W. & ABART, R. (eds): *Mineral reaction kinetics: Microstructures, textures, chemical and isotopic signatures*. *EMU Notes in Mineralogy* **14,** 469–540. https://doi.org/10.1180/EMU-notes.16.14

GIERÉ, R. 1986: Zirconolite, allanite and hoegbomite in a marble skarn from the Bergell contact aureole: implications for mobility of Ti, Zr and REE. – *Contribution to Mineralogy and Petrology* **93,** 459–470. https://doi.org/10.1007/BF00371716

GIERÉ, R. 1990: Hydrothermal mobility of Ti, Zr and REE: examples from the Bergell and Adamello contact aureoles (Italy). – *Terra Nova* **2,** 60–67. https://doi.org/10.1111/j.1365-3121.1990.tb00037.x

GIERÉ, R. & WILLIAMS, C.T. 1992: REE-bearing minerals in a Ti-rich vein from the Adamello contact aureole (Italy). – *Contribution to Mineralogy and Petrology* **112,** 83–100. https://doi.org/10.1007/BF00310957

GIERÉ, R., WILLIAMS, C.T. & LUMPKIN, G.R. 1998: Chemical characteristics of natural zirconolite. – *Schweizerische Mineralogische und Petrographische Mitteilungen* **78,** 433–459. https://doi.org/10.5169/seals-59299

GUZMICS, T., ZAJACZ, Z., MITCHELL, R.H., SZABÓ, CS. & WALLE, M. 2015: The role of liquid–liquid immiscibility and crystal fractionation in the genesis of carbonatite magmas: insights from Kerimasi melt inclusions. – *Contribution to Mineralogy and Petrology* **169,** 17. https://doi.org/10.1007/s00410-014-1093-4

HAIFLER, J., ŠKODA, R., FILIP, J., LARSEN, A.O. & ROHLÍČEK, J. 2021: Zirconolite from Larvik Plutonic Complex, Norway, its relationship to stefanweissite and nöggerathite, and contribution to the improvement of zirconolite endmember systematic. – *American Mineralogist* **106,** 1255–1272. https://doi.org/10.2138/am-2021-7510

HALÁSZ, N., BERKESI, M., TÓTH, M., MITCHELL, R.H., MILKE, R. & GUZMICS, T. 2023: Reconstruction of magma chamber processes

preserved in olivine-phlogopite micro-ijolites from the Oldoinyo Lengai, Tanzania. – *Journal of African Earth Sciences* **197,** 104738. https://doi.org/10.1016/j.jafrearsci.2022.104738

Heaman, L.M. & Le Cheminant, A.N. 1993: Paragenesis and U–Pb systematics of baddeleyite (ZrO). – *Chemical Geology* **110,** 95–126. https://doi.org/10.1016/0009-2541(93)90249-I

Hiroi, Y., Motoyoshi, Y., Shiraishi, K. & Mathavan, V. 1997: Local formation of hercynite–plagioclase symplectite after garnet and sillimanite in khondalite from Habarana, Sri Lanka: mineral textures. – *Proc NIPR Symposium, Antarctic Geoscience* **10,** 153–164. https://doi.org/10.2465/jmps.221130

Hoffman, J.D. & Weeks, J.J. 1962: Rate of spherulitic crystallization with chain folds in polychlorotrifluoroethylene. – *Journal of Chemical Physics* **37,** 17–23. https://doi.org/10.1063/1.1733363

Hurai, V., Huraiová, M., Gajdošová, M., Konečný, P., Slobodník, M. & Siegfried, P.R. 2018: Compositional variations of zirconolite from the Evate apatite deposit (Mozambique) as an indicator of magmatic-hydrothermal conditions during post-orogenic collapse of Gondwana. – *Mineralogy and Petrology* **112,** 279–296. https://doi.org/10.1007/s00710-017-0538-7

Káldos, R., Mitchell, R.H., Dawson, J.B., Milke, R. & Szabó, Cs. 2015: A melt evolution model for Kerimasi volcano, Tanzania: Evidence from carbonate melt inclusions in jacupirangite. – *Lithos* **238,** 101–119. https://doi.org/10.1016/j.lithos.2015.09.011

Keller, J. & Kraft, M. 1990: Effusive natrocarbonatite activity of Oldoinyo Lengai, June 1988. – *Bullettin Volcanology* **52,** 629–645. https://doi.org/10.1007/BF00301213

Kesson, S.E., Sinclair, W.J. & Ringwood, A.E. 1983: Solid solution limits in SYNROC zirconolite. – *Waste Management* **4,** 259–265. https://doi.org/10.1016/0191-815X(83)90019-0

Klaudius, J. & Keller, J. 2006: Peralkaline silicate lavas at Oldoinyo Lengai, Tanzania. – *Lithos* **91,** 173–190. https://doi.org/10.1016/j.lithos.2006.03.017

Kruk, M.N., Doroshkevich, A.G., Prokopyev, I.R. & Izbrodin, I.A. 2021: Mineralogy of phoscorites of the Arbarastakh Complex (Republic of Sakha, Yakutia, Russia). – *Minerals* **11,** 556. https://doi.org/10.3390/min11060556

Lithgow-Bertelloni, C. & Silver, P.G. 1998: Dynamic topography, plate driving forces and the African Superswell. – *Nature* **395,** 269–272. https://doi.org/10.1038/26212

Lumpkin, G.R., Smith, K.L., Blackford, M.G., Gieré, R. & Williams, C.T. 1994: Determination of 25 elements in the complex oxide mineral zirconolite by analytical electron microscopy. – *Micron* **25,** 581–587. https://doi.org/10.1016/0968-4328(94)90020-5

Mana, S., Furman, T., Carr, M.J., Mollel, G.F., Mortlock, R.A., Feigenson, M.D., Turrin, B.D. & Swisher, C.C. 2012: Geochronology and geochemistry of the Essimingor volcano: Melting of metasomatized lithospheric mantle beneath the North Tanzanian Divergence zone (East African Rift). – *Lithos* **155,** 310–325. https://doi.org/10.1016/j.lithos.2012.09.009

Mana, S., Furman, T., Turrin, B.D., Feigenson, M.D. & Swisher, C.C. 2015: Magmatic activity across the East African North Tanzanian Divergence Zone. – *Journal of the Geological Society* **172,** 368–389. https://doi.org/10.1144/jgs2014-072

Marxsen, S.F., Häu ler, M., Mecking, S. & Alamo, R.G. 2020: Isothermal step thickening in a long-spaced aliphatic polyester. – *Polymer* **191,** 122282. https://doi.org/10.1016/j.polymer.2020.122282

Mazzi, F. & Munno, R. 1983: Calciobetafite (new mineral of the pyrochlore group) and related minerals from Campi Flegrei, Italy; crystal structures of polymignyte and zirkelite: comparison with pyrochlore and zirconolite. – *American Mineralogist* **68,** 262–276.

Mitchell, R.H. 2002: *Perovskites: modern and ancient.* – Almaz Press, Ontario/CA, 316 p.

Mitchell, R.H. & Vladykin, N.V. 1993: Rare earth element-bearing tausonite and potassium barium titanites from the Little Murun potassic alkaline complex, Yakutia, Russia. – *Mineral Magazine* **57,** 651–664. https://doi.org/10.1180/minmag.1993.057.389.09

Mororó, E.A.A., Berkesi, M., Zajacz, Z. & Guzmics, T. 2024: Rare earth element transport and mineralization linked to fluids from carbonatite systems. – *Geology* **52,** 240–244. https://doi.org/10.1130/G51531.1

Obata, M. 2011: Kelyphite and symplectite: textural and mineralogical diversities and universality, and a new dynamic view of their structural formation. – In: Sharkov, E.V. (eds.): *New Frontiers in Tectonic Research–General Problems, Sedimentary Basins and Island Arcs. InTech* Open, 93–122. https://doi.org/10.5772/20265

Pouchou, J.L. & Pichoir, F. 1991: Quantitative analysis of homogeneous or stratified microvolumes applying the model 'PAP'. – In: Heinrich, K.F.J. & Newbury D.E. (eds): *Electron probe quantitation*. Plenum Press, New York/NY, 31–75.

Prodehl, C., Jacob, B., Thybo, H., Dindi, E. & Stangl, R. 1994: Crustal structure on the northeastern flank of the Kenya rift. – In: Prodehl, C., Keller, G.R. & Khan, M.A. (eds): Crustal and Upper Mantle Structure of the Kenya Rift. *Tectonophysics* **236,** 271–290. https://doi.org/10.1016/0040-1951(94)90180-5

Rasmussen, B. & Fletcher, I.R. 2004: Zirconolite: A new U–Pb chronometer for mafic igneous rocks. – *Geology* **32,** 785–788. https://doi.org/10.1130/G20658.1

Ried, F. 1994: *Titanmobilität: Metasomatische, titanreiche Adern am Kontakt von Dolomitmarmoren zur Bergell Intrusion*. – PhD thesis, ETH Zürich, Zürich/CH, 204 p.

Rogers, N., Macdonald, R., Fitton, G., George, R., Smith, M. & Barreiro, B. 2000: Two mantle plumes beneath the East-African rift system: Sr, Nd, and Pb isotope evidence from Kenya Rift basalts. – *Earth and Planetary Science Letters* **176,** 387–400. https://doi.org/10.1016/S0012-821X(00)00012-1

Rossell, H.J. 1980: Zirconolite – a fluorite-related superstructure. – *Nature* **283,** 282–283. https://doi.org/10.1038/283282a0

Sekisova, V.S., Sharygin, V.V., Zaitsev, A.N. & Strekopytov, S. 2015: Liquid immiscibility during crystallisation of forsterite–phlogopite ijolites at Oldoinyo Lengai Volcano, Tanzania: study of melt inclusions. – *Russian Geology and Geophysics* **56,** 1717–1737. https://doi.org/10.1016/j.rgg.2015.11.005

Simiyu, S.M. & Keller, G.R. 1997: An integrated analysis of lithospheric structure across the East African plateau based on gravity anomalies and recent seismic studies. – *Tectonophysics* **278,** 291–313. https://doi.org/10.1016/S0040-1951(97)00109-1

Smith, K.L. & Lumpkin, G.R. 1993: Structural features of zirconolite, hollandite and perovskite, the major waste-bearing phases in

Synroc. – In: BOLAND, J.N. & FITZGERALD, J.D. (eds): *Defects and Processes in the Solid State. Geoscience Applications*, Elsevier, Amsterdam, 401 p.

VANCE, E.R., BEGG, B.D., DAY, R.A. & BALL, C.J. 1994: Zirconolite-rich ceramics for actinide wastes. – *Materials Research Society Symposium Proceedings* **353,** 767–774. https://doi.org/10.1557/PROC-353-767

VEKSLER, I.V. & TEPTELEV, M.P. 1990: Conditions for crystallization and concentration of perovskite-type minerals in alkaline magmas. – *Lithos* **26,** 177–189. https://doi.org/10.1016/0024-4937(90)90047-5

VERNON, R.H. 2004: *A practical guide to rock microstructure.* – Cambridge University Press, Cambridge, UK, 606 p.

WANG, N., MAO, Q., ZHANG, T., HAO, J. & LIN, Y. 2021: NanoSIMS and EPMA dating of lunar zirconolite. – *Earth Planet Space* **8,** 51. https://doi.org/10.1186/s40645-021-00446-3

WEEKS, J.J. 1963: Melting temperature and change of lamellar thickness with time for bulk polyethylene. – *Journal of Research of the National Bureau of Standards, Section A: Physics and Chemistry* **67,** 441–451. https://doi.org/10.6028/jres.067A.046

WHITE, T.J. 1984: The microstructure and microchemistry of synthetic zirconolite, zirkelite and related phases. – *American Mineralogist* **69,** 1156–1172.

WHITE, T.J., SEGALL, R.L., HUTCHINSON, J.L. & BARRY, J.C. 1984: Polytypic behaviour of zirconolite. – *Proceedings of the Royal Society A: Mathematical, Physical and Engineering Sciences* **392,** 343–358. https://doi.org/10.1098/rspa.1984.0035

WHITNEY, D. & EVANS, B.W. 2010: Abbreviations for names of rock-forming minerals. – *American Mineralogist* **95,** 185–187. https://doi.org/10.2138/am.2010.3371

WILLIAMS, C.T. & GIERÉ, R. 1996: Zirconolite: A review of localities worldwide, and a compilation of its chemical compositions. – *Bulletin of the Natural History Museum, London* **52,** 1–24.

WILLIAMS, C.T., BULAKH, A.G., GIERÉ, R., LUMPKIN, G.R. & MARIANO, A.N. 2001: Alteration features in natural zirconolite from carbonatites. – *Materials Research Society Symposium Proceedings* **663,** 945. https://doi.org/10.1557/PROC-663-945

WOOD, J. & GUTH, *A. 2014: East Africa's Great Rift Valley: a complex rift system. Michigan Technological University*. http://geology.com/articles/east-africa-rift.shtml (accessed 16.02.2025)

XIROUCHAKIS, D., LINDSLEY, D.H. & ANDERSEN, D.J. 2001: Assemblages with titanite (CaTiOSiO), Ca–Mg–Fe olivine and pyroxenes, Fe–Mg–Ti oxides, and quartz: Part I. Theory. – *American Mineralogist* **86,** 247–253. https://doi.org/10.2138/am-2001-2-306

XIROUCHAKIS, D., LINDSLEY, D.H. & ANDERSEN, D.J. 2001: Assemblages with titanite (CaTiOSiO), Ca–Mg–Fe olivine and pyroxenes, Fe–Mg–Ti oxides, and quartz: Part II. Application. – *American Mineralogist* **86,** 254–264. https://doi.org/10.2138/am-2001-2-307

YAXLEY, G.M., ANENBURG, M., TAPPE, S., DECREE, S. & GUZMICS, T. 2022: Carbonatites: classification, sources, evolution, and emplacement. – *Earth and Planetary Science Letters* **50,** 261–293. https://doi.org/10.1146/annurev-earth-032320-104243

YUAN, X., YANG, Z., MAYANOVIC, R.A. & HOU, Z. 2024: Experimental evidence reveals the mobilization and mineralization processes of rare earth elements in carbonatites. – *Science Advances* **10/27,** eadm9118 https://doi.org/10.1126/sciadv.adm9118

ZUBKOVA, N.V., CHUKANOV, N.V., PEKOV, I.V., TERNES, B., SCHÜLLER, W., KSENOFONTOV, D.A. & PUSHCHAROVSKY, D.Y. 2018: The crystal structure of nonmetamict Nb-rich zirconolite-3T from the Eifel paleovolcanic region, Germany. – *Zeitschrift für Kristallographie – Crystalline Materials* **7,** 463–468. https://doi.org/10.1515/zkri-2017-2133

Manuscript received: 23/01/2026